

Chapter 4

The AOCS Functions

Abstract This chapter presents the operating modes of a typical modern satellite attitude control system (AOCS). The various modes are presented in terms of functional requirements, H/W architecture, functional block diagram and controller characteristics. The control mode dynamics are described through various simulations.

4.1 Introduction

This chapter presents the operating modes of a typical modern satellite attitude and orbit control system (AOCS). After a description of the mission phases and the AOCS functional blocks, the various modes are presented in terms of functional requirements, H/W architecture, functional block diagram and controller characteristics. The control mode dynamics are described through various simulations.

Over the last 40 years many different AOCS architectures have been proposed and developed for different applications (i.e. telecommunications, scientific, Earth observation...).

A full review of all possible design being impossible, we have decided to present a *multi-mission* architecture, conceived to be flexible to implement most of the requirements in existing applications. This architecture is not a real AOCS, specific adaptations in terms of equipment and design must be introduced to cope with the different orbits or some specific requirements. However this concept allows to introduce the discussion on a wide class of design issues and any specificity will be highlighted as necessary. The design solutions presented are not unique, we can also have different design implementations with respect to those presented to respond to specific needs.

In the last years, due to the high level of flexibility, autonomy and processing capability embedded in the avionic sensors and on-board software (OBS), the avionic solutions converge to a small number of possibilities which can be reused in different contexts. It is then possible to talk about a *multi-mission avionic bus*, able to fulfill all most important AOCS requirements.

The three axis stabilized attitude and orbit control system architecture shown in Sect. 4.3 is able to re-orient the spacecraft in a predefined target attitude from a

nominal Nadir pointing attitude (that is to maintain **BRF** rotated with respect to **ORF** of some target Euler angles).

Depending on the P/L different spacecraft attitudes can be desired:

- *Earth pointing: geocentric or geodetic;*
- *Sun pointing;*
- *inertial pointing;*
- *roll/pitch/yaw offset* and bias capability.

Moreover this AOCS architecture can implement different steering pointing maneuvers. Specific steering maneuvers are required to support the payload or the spacecraft according to different mission needs such as:

- maintain the solar array wings orthogonal to the Sun direction (in order to maximize the generation of power);
- steer the yaw angle during the orbit (to maximize the sun input on the solar arrays in inclined orbits or to compensate the doppler shift due to the Earth motion for a SAR satellite);
- bias attitude in roll (to re-point the bore-sight of an optical/radar/transmitter payload);
- bias attitude in pitch (to re-point the bore-sight of an optical/radar/transmitter payload);
- steer attitude to point different ground targets;
- maintain an inertial attitude (e.g. long firing maneuver, star imaging);

The torque produced by the reaction wheels (or CMG when high agility is required) mounted in pyramidal configuration (see Chap. 9 for the different RW configurations), allows the spacecraft to perform re-pointing maneuvers. The attitude is measured with star trackers and the angular rate with three axes gyroscopes. Low noise sensors and actuators, a stiff structure and a properly designed control logic guarantee a very stable platform with precise pointing (mandatory characteristics for missions adopting high performance optical sensors or synthetic aperture radar).

In telecommunication missions that usually require less demanding performances the same architecture may be used by changing the class and the cost of sensors and actuators.

The AOC system is designed to perform the orbit correction maneuvers required by the mission. The first orbital maneuvers are those to correct orbital errors due to the launcher's mis-performance in releasing the satellite in the nominal separation orbit, after those to acquire/achieve/maintain the specified operational orbit are performed, to finish with de-orbiting maneuvers at the end of the satellite's life.

These maneuvers are implemented using the on-board propulsion subsystem. Different architectures and propulsion technologies can be used, see Chap. 8 for a survey on these technologies.

4.2 Typical Mission Profiles for LEO and GEO Mission

In most LEO missions (typically Earth observation missions) the launch vehicle (LV), after lift-off and after its cruise mode, releases the satellite in an injection orbit close to the operational one with a predefined attitude and a residual angular rate agreed upon by the launch authority and the owner of the satellite.

In the GEO mission case (typically a telecommunication mission), the launch vehicle after lift-off and after its cruise mode releases the satellite in a parking orbit (i.e. GTO—geostationary transfer orbit) that is not the operational orbit and therefore the satellite has to perform some long thruster firings with its own propulsion system (chemical or electrical), in order to reach the operational target orbit.

The mission profiles for LEO and GEO have a different *launch and early orbit phase* (LEOP) approach and AOCS has to be designed to support the specific LEOP profile. Moreover, AOCS has to be designed to support all mission's needs from LEOP to satellite disposal. The satellite must implement at least the following operational phases: *launch phase, transfer phase, deployment phase, mission phase, deorbit phase*. Each phase is supported by one or more AOCS modes. The transition between different modes is carried out by the on-board software (OBS) upon receiving a ground telecommand or when triggered by a timer.

Launch Phase

The launch phase is supported by the AOCS implementing an idle operational mode that is the only AOC mode allowed during the satellite launch mode. In idle mode no attitude control is realized. Only satellite survival activities are carried out during this phase (e.g. active thermal control). The avionic must implement multiple H/W barriers in order to prevent dangerous unwanted events in the launcher fairing, like thrusters activations or deployments.

A robust logic has to be implemented to detect and confirm the satellite's separation from the launcher.

Transfer Phase

Transfer phase is a pre-operational phase lasting from the launcher separation to the acquisition of the operational orbit. The transition from launch phase to transfer phase is typically autonomously realized by software as soon as separation from the launcher is detected. In this phase AOCS functions are required to damp the initial LV separation rates,¹ acquire an attitude with positive power balance (Sun acquisition) and realize if necessary a series of orbital maneuvers to reach the final operational orbit.

The rate damping and *safe* attitude pointing can be achieved according to a specific AOC design. Different schemes and different sensors/actuators can be used by AOC control loop to reach this objective. In this chapter two possible designs are presented

¹The separation rates can be quite high such as 1–2 deg/s.

such as the *safe hold mode* (SHM) and the *Sun acquisition mode-emergency mode* (SAM-EM).

The main goal of this mode is to be simple and reliable. This implies using a minimal hardware and a simple logic that guarantees a convergence of the loop starting from *any reasonable* initial attitudes and rates.

In case of GEO missions the transfer phase is maintained until reaching the target orbit. Then deployment phase is entered upon receiving a telecommand.

The classic approach of the orbital transfer to GEO (for a description of the control modes and phases of a classic telecom satellite see [1]) implements a sequence of firings of a liquid apogee engine (LAE). The attitude in this mode is controlled such to point the LAE thrust vector along the optimal direction. The number of firings depends on the transfer orbit strategy selected by mission operation engineers and usually requires more than one transition into *orbit control mode* (usually two or three apogee boosts).

The theory of optimal orbital transfers presented in Sect. 7.8 can be used to determine the optimal firing direction.

In more recent design approaches these transfers are realized using low thrust plasmic thrusters continuously firing for very long durations. The theory of this kind of optimal transfer is studied in Sect. 7.9.

During firings that last many orbits the AOCS will continuously align the firing thruster along the optimal direction (which rotates continuously in **ORF**) and will rotate the satellite and the solar arrays in order to maximize the solar power input. In these missions the deployment phase is anticipated before the transfer phase.

Deployment Phase

The deployment phase is normally entered when the satellite has finally reached the target orbit (i.e. after the LV separation in LEO/MEO missions or after the transfer orbit in GEO missions). In this phase all satellite's appendages (i.e. solar arrays, antennas, instruments) will be deployed. The AOC mode used to deploy all appendages is selected considering the dynamic conditions and the thermal and power constraints.

Mission Phase

The mission phase is entered after the deployment and it is maintained up to the *end of mission* before satellite disposal. In this phase AOC system has to support all nominal operations required by the satellite. Basically the *nominal pointing mode* (i.e. mission mode) is designed to achieve a good attitude pointing accuracy and knowledge necessary for the correct payload operations. Specific functions linked to the payload requirements are implemented in this phase like agile pointing or steering capability. Moreover, AOCS is also required to support station keeping maneuvers necessary to maintain the satellite in the correct orbital box (i.e. GEO mission) or close to the correct reference orbit (i.e. LEO mission). This objective is achieved through an orbit control mode capable to implement the required *DV* maneuvers.

Deorbit Phase

This phase is entered when the satellite reaches its *end of mission* because consumable resources are going to finish and the owner decides to de-orbit the satellite. The AOC has to implement the *DV* maneuver to transfer the satellite into its graveyard orbit (GEO missions) or decaying orbit (LEO missions), following the rules of the *international space law*.

We have briefly seen the AOCS modes and functions that must be designed. Each AOCS mode can be present in different mission phases. The following section discusses the control modes mainly in terms of their software architecture and data flow.

4.3 Control Modes Architecture

Generally a control mode is designed to support different mission phases and each mode can be divided into several sub-modes. Each mode is characterized by its own set of H/W on control (H/W that is actively used by the on-board software to implement the control loop).

Transitions from one control mode to another are commanded either by dedicated ground telecommands (TC) or by automatic recovery actions activated by the detection of an on-board equipment failure.

The functions fulfilled by the AOCS control system are coded inside periodic tasks executed by the on-board S/W in a time cycle that is generally in the range of 50–500 ms. The time cycle must be fast enough to represent the dynamics and the bandwidth of the controller, taking into account the constraints of the available processing resources and the sensor and actuators measurement and execution delays. The discretization of the control algorithms is therefore an important subject for any on-board real-time control system like AOCS.

The control mode periodic tasks (see Fig. 4.1) can be grouped into:

- *pre-processing function*. It is in charge of processing the raw data acquired from sensors in order to make them available to the control system every time cycle.
- *orbital pre-processing function*. It is in charge of providing orbital and time information to all on-board subsystems.
- *attitude determination function*. It is in charge of providing both S/C attitude and attitude error information. The attitude error will be used by the operational mode controller to implement the control law required by the mode.
- *mode management function*. Depending on the current operational phase mode management function is in charge of implementing the actual control law defining the control command.
- *post-processing function*. This function is in charge of representing the control command in raw data suitable for the AOCS actuators (RW motor voltages, RCT valves on-time...).

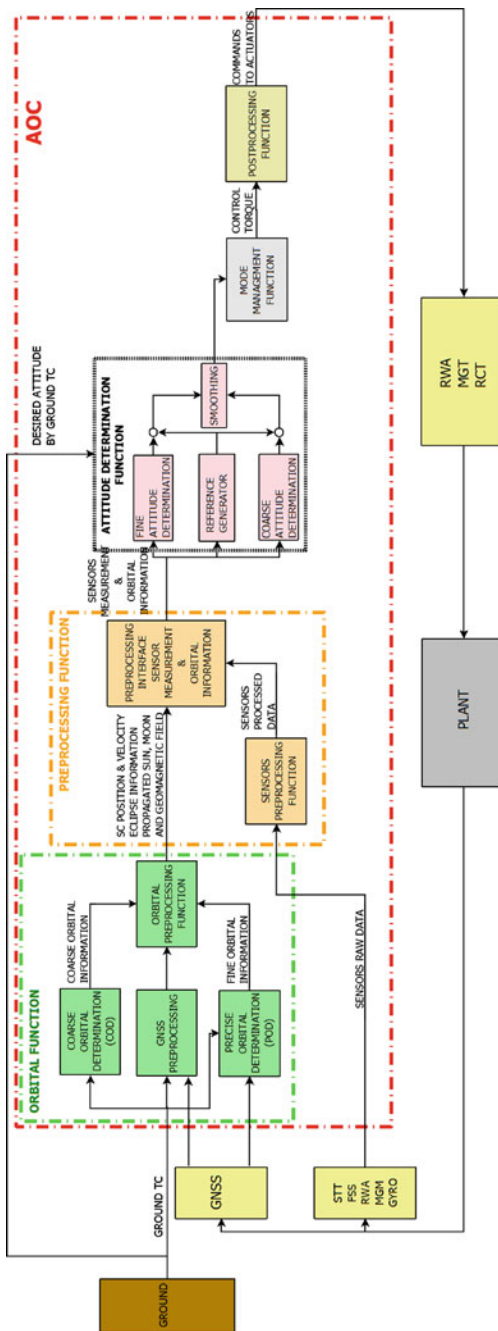


Fig. 4.1 AOCS functional data flow

4.3.1 Mode Management Function

The mode management function is in charge to implement AOC operating modes and submodes and the appropriate AOC transition logic between the current AOC mode/submode and the new AOC mode/submode.

All AOC transitions can be triggered either during the nominal mission operation using ground telecommands, or following a recovery action due to a software or a hardware alarm. Moreover, the mode management function is in charge of implementing the actual control laws that define the control actions. In Sect. 4.4 a description of AOC modes' algorithms is given.

A possible operating mode chart is shown in Fig. 4.2. As already said, the transitions between the various AOCS modes can start due to a ground telecommand (TC) or the detection of a on-board failure (FDIR). The operating mode used during the launch phase is the *idle mode*. This mode is autonomously entered by the software as soon as the separation from the launcher is detected by a hardware switch.

This mode is a stand-by mode in which the on-board Computer (OBC) is active but actuators are inhibited and no attitude control is applied. The internal states of all subsystems including the avionic are packed and formatted in a digital telemetry stream by the on-board Computer (OBC) software and down-linked to the ground station for analysis. This telemetric process is common to all operating modes which must provide an overall observability such to guarantee suitable reaction times to

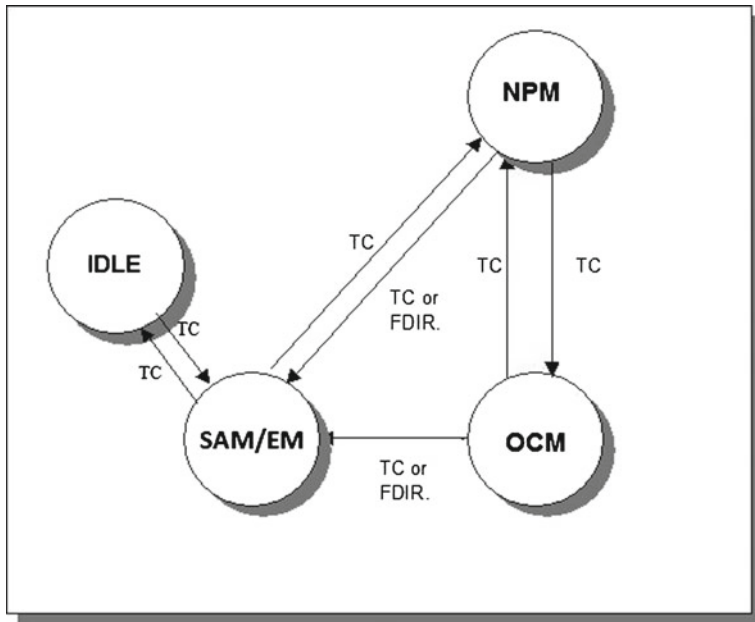


Fig. 4.2 Typical AOCS modes transition logic

the ground station in case anomalies or failures occur. The telemetric data rate is an important difference between LEO and GEO satellites. LEO satellites, in general, have short and periodic contact periods (a few minutes per passage) with the ground stations and therefore need higher telemetry data rates (in the range of many Mbit/s) while the GEO satellites are characterized by continuous contact periods and need much slower data rates (in the range of 10–100 Kbit/s). In addition, LEO satellites normally store the on-board states in dedicated memories in order to make available to ground a historic file of the satellite internal states.

In the *multimission avionic* two operating modes, the *Sun acquisition mode-emergency mode* (SAM-EM) and the *safe hold mode* (SHM)—this second mode only for LEO satellites—are foreseen for the pre-operational phase, when the objective is to charge the satellite's batteries by pointing the solar arrays towards the Sun and to maintain an attitude which allows a good telecommand and telemetric flow with the ground station in order to check the health of the on-board instruments. The same modes are typically used also in contingency cases (i.e. after a failure).

While the SAM-EM mode is used in all operational orbits, the SHM is a mode used only in LEO Sun Synchronous orbit (SSO) because it needs to operate in quite a strong environmental magnetic field.

The SAM-EM is designed to orient the spacecraft in a safe Sun-pointing three-axes controlled attitude. This mode is nominally entered by a ground telecommand (TC) during the pre-operational phase. Moreover, it is the first recovery mode entered autonomously by the software when a hardware failure occurs. The SAM-EM mode design is carried out to minimize the transient acquisition phase and provide a fast, steady state attitude acquisition. This mode uses the Sun sensor, magnetometer (only in LEO orbits), gyro and a coarse orbit determination (COD) algorithm. The actuation is carried out with the reaction wheels (RW). The magneto-torquers (MGT) are used in LEO orbits to unload wheel momentum when reaction wheels reach a certain maximal speed. In GEO orbits the same momentum unload is realized using reaction control thrusters (RCT).

The SHM is a robust mode specific of LEO SSO orbit conditions that guarantees extremely long survival periods using a minimum set of actuators and sensors: only magnetometer (MGM), MGT and RW.

The *normal pointing mode* (NPM), is designed to achieve a fine pointing attitude with a specified accuracy during the operational phase. This mode implements a fine three axes attitude control, suitable for payload imaging operations using Star trackers and gyro sensors.

Some new NPM mode designs may implement also gyro-less controllers using only star trackers for angular and rate feedback. With the present star tracker technology the gyro less approach can be widely applied unless there are very demanding stability and agility requirements.

The precise orbit determination (POD) is used in order to transform the inertial attitude information of the star tracker into **ORF** attitude error. As in the SAM-EM, reaction wheels are used for torque actuation and MGT (in LEO) or RCT (in GEO) for wheel momentum unloading. The NPM is the nominal mode during the payload operations and all features and requirements needed for the achievement of

the operational mission conditions dictated by the specific payload characteristics must be considered in the design phase.

In order to perform the orbital maneuvers a dedicated operational mode is designed: the *orbit control mode* (OCM) which is able to handle arbitrary attitude slews in order to align the propulsion system thrust vector in the desired direction according to the requested maneuver acceleration profiles (see Chap. 7).

All these modes are nominally entered by ground TCs. At mode entry point, AOCS autonomously re-configures the equipment requested for the new mode. A possible attitude control mode transition logic is shown in Fig. 4.2.

4.3.2 Pre-processing Function

The pre-processing function is in charge to process all sensors and actuators sampled raw data for any AOC mode. The pre-processing algorithms transform all data coming from sensors (i.e. gyro, GPS receiver, Star tracker, MGM, FSS) and actuators (i.e. RWA) into data usable by the controller.

The sensor raw data will be subjected to at least format conversion, reference frame transformation (from sensor frame to **BRF**), calibration, filtering and any other processing necessary to provide a proper input to the algorithms implementing attitude and orbit determination and operational mode management.

It distributes the necessary sensor information to the other on-board functions (i.e. telemetry or FDIR functions).

4.3.3 Post-processing Function

The post-processing function has in charge to process all command data produced by the controller and to transform them into data accepted by the relevant sensors and actuators used in each AOC mode.

The post-processing function elaborates the high level actuation information produced by the mode management function in each AOC mode and converts them into the actuators' input format. The actuators high level commands produced by the controller will be subject to at least reference frame transformation (from **BRF** to actuator frame), calibration and format conversion plus any other processing necessary to provide a proper input.

4.3.4 Orbital Pre-processing Function

The orbital pre-processing function is designed to provide the orbital information (i.e. at least satellite position, velocity and time) to all other on-board AOC functions.

The orbit determination task can be implemented autonomously on-board using a *global navigation system* (GNSS) receiver (see Chap. 9), or by the ground station (G/S) using the two way ranging measurements produced by the telemetry telecommand link. The first methodology is preferred in the LEO missions where the visibility of the GNSS constellations is good while the visibility of the G/S is short and infrequent, the second methodology is used mainly in GEO missions where the conditions are opposite. It is only recently that GEO missions using GNSS receivers receiving the signals of the GNSS satellites visible behind the Earth have been proposed in order to augment the autonomy of the satellite in the case of very long LEOP with low thrust transfer.

When G/S calculates the orbit an on-board propagator is periodically updated by TC in order to align it with the real orbit.

When the orbit determination is realized through the on-board processing of a global navigation system (GNSS) receiver data, AOCS implements a real time precise orbit determination (POD) based on a navigation *extended Kalman filter* (EKF), using a prediction correction approach (see [2] which deals also with navigation filters). The POD has access to the output of the GNSS receiver and uses an EKF in order to improve the accuracy of the GNSS measurement by precisely modeling the reference orbit, including perturbation models for atmospheric drag and geo-potential. This precise orbital propagator produces the best orbit knowledge available on-board.

The POD calculates the orbital data in terms of spacecraft orbital position and velocity. As a reference, typical position and velocity errors about all **ECI** axes are shown in Figs. 4.3 and 4.4 for a real time on-board estimator in a LEO SSO orbit.

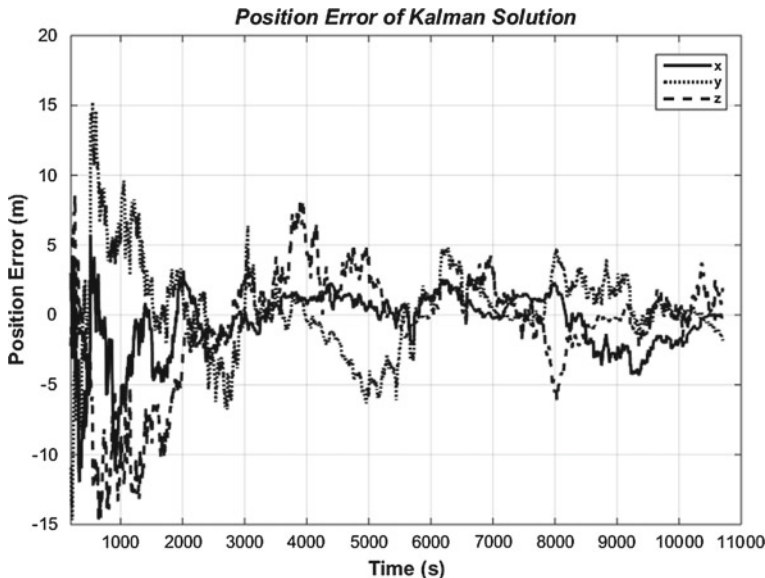


Fig. 4.3 POD EKF 3 axes position error

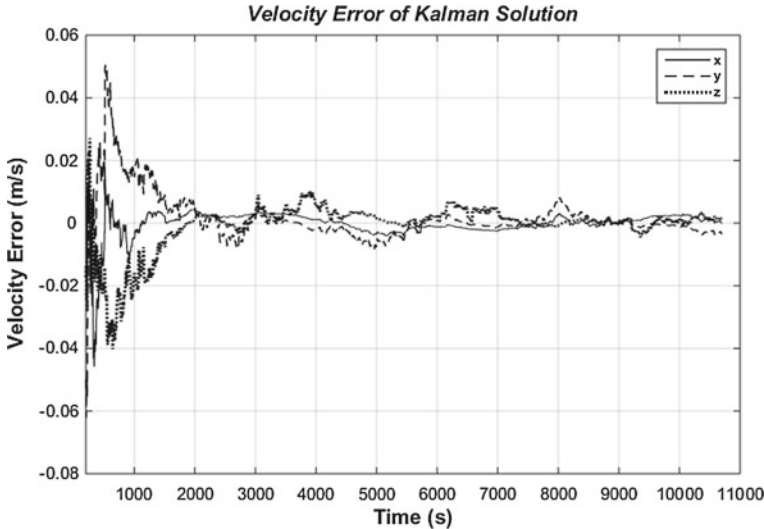


Fig. 4.4 POD EKF 3 axes velocity error

In case of double failure of the GNSS receiver, the POD can be used in a degraded mode in which it produces its output, propagating a set of orbit states periodically up-linked by ground. This back up use of POD in LEO is similar to that of GEO missions and the orbit state is produced with the available G/S ranging measurements.

The AOCS may implement also a coarse orbit propagator (COD) which propagates a coarse spacecraft's position and velocity starting from the initial information uploaded periodically by ground. It is used when there is no much need of accuracy or a limited availability of OBC processing resources (CPU time, memory).

4.3.5 Attitude Determination Function

The attitude determination function implements the algorithms (see [3]) that are designed to provide the attitude estimation necessary to feed attitude controllers. These algorithms, when optimal estimates are necessary can be improved using the method that is briefly presented in Sect. 5.3, where kalman filters introduce the satellite dynamic information to implement an optimal estimation (see [4, 5]). We can have coarse as well as fine attitude estimators, depending on the mission phase and the required attitude pointing performance. The fine and the coarse attitude determination algorithms are implemented typically in a single module together with a reference attitude generator.

By comparing the attitude estimate with the reference attitude this module provides the attitude error estimate to the operational mode controller (see Fig. 4.5).

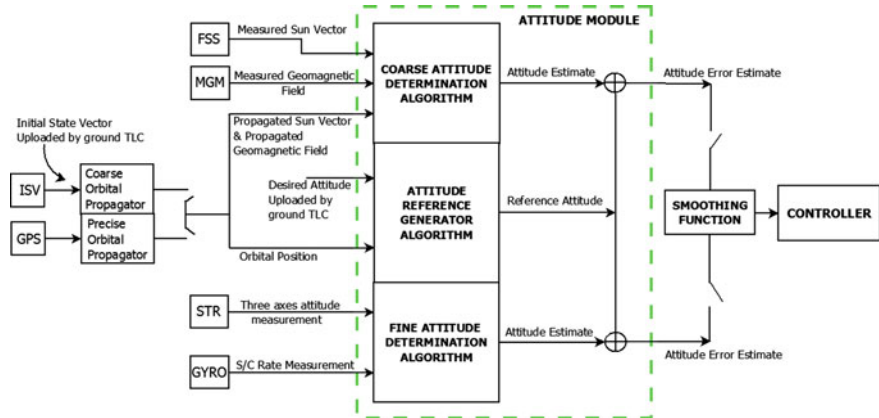


Fig. 4.5 Attitude determination functional flow

The coarse and fine attitude determination algorithms are fully interchangeable. The first one is used during the SHM or SAM-EM when the main goal is to re-orient the spacecraft in a safe attitude, while the second one is used during the mission phases when it is necessary to reach a high pointing accuracy and a high level of maneuverability relying on a very agile and flexible attitude control system.

In the *multimission avionic* the coarse attitude algorithm is a *Triad-like* algorithm (see for example [3, 6, 7]) that estimates the spacecraft attitude using the low accuracy sensor (Sun sensor and magnetometer) as well as the COD.

The fine attitude determination algorithm is an attitude estimation algorithm based on the gyro and star tracker measurement. Combining the gyro and the star tracker measurements, using a prediction correction approach, this algorithm smooths the noisy measurements and provides the best attitude estimate available on-board.

The fine attitude determination algorithm is designed to work with one, two or even three star tracker sensors both in hot and cold redundancy, the sensor configuration depending on the level of the desired accuracy and the study of the star tracker blinding conditions from the Sun, the Earth and the Moon (see Chap. 9). In case of star tracker unavailability (temporary blinding conditions), the algorithm autonomously propagates the last attitude estimate with the gyro rate until the star tracker measurement is available again.

The reference attitude is calculated by the attitude reference generator algorithm which uses the orbital information, coming from the COD/POD. This algorithm, properly configured, is able to generate a variety of attitude maneuver profiles. Depending on the mission needs, minimum jerk maneuver, minimum time maneuver, roll, pitch, yaw offsets and periodic maneuvers can be implemented. Moreover a fully customized maneuver made up of polynomial and harmonic profiles can be configured by ground telecommand.

The interchangeability of coarse and fine algorithms, the presence of a coarse and fine orbital propagator and the possibility of a temporary star tracker unavailability lead to the design of a smoothing module. Every time a change in the orbital reference or in the measurement occurs, the software autonomously performs a smooth transition, using a dedicated weighting function, to minimize the attitude transient.

4.3.5.1 Coarse Attitude Determination Algorithm

The coarse attitude determination function provides a coarse attitude estimate with the construction of two triads of orthonormal unit vectors using the Sun sensor and magnetometer measurement as well as the coarse orbit propagator information. This method is the so-called *Triad* algorithm. This kind of implementation is typical of LEO orbits; in GEO orbits, where the magnetic field is too low for a reliable attitude measurement, it is typical to implement a different algorithm that uses the Sun sensor and the gyro data to compute the attitude in the two directions orthogonal to the Sun's one, while the attitude along the Sun's direction, that cannot be resolved in absolute terms, is determined with respect to some initial constant. The partial attitude observability that results must be taken into account in the design of GEO acquisition modes.

The attitude determination problem is equivalent to determine in real time the attitude rotation matrix $M_{B \leftarrow O}$ that describes the orientation of the spacecraft **BRF** with respect to the **ORF**.

Let's indicate

- s_{BRF} Sun unit vector measured by the Sun sensor;
- m_{BRF} magnetic field unit vector measured by the magnetometer sensor;
- s_{ORF} Sun unit vector provided by orbital propagator;
- m_{ORF} magnetic field unit vector provided by orbital propagator.

where s_{BRF} and m_{BRF} refer to **BRF** components, while s_{ORF} and m_{ORF} refer to **ORF** components.

The following relations follow from the definition of the attitude matrix, if we assume for the moment a null measurement error:

$$\begin{aligned} s_{BRF} &= M_{B \leftarrow O} s_{ORF} \\ m_{BRF} &= M_{B \leftarrow O} m_{ORF} \end{aligned} \tag{4.1}$$

We define now the following orthogonal unit vectors of a new orthogonal triad **TRD**, in **BRF** and **ORF** components:

$$\begin{aligned}
t_{1_{BRF}} &= s_{BRF} \\
t_{2_{BRF}} &= \frac{s_{BRF} \times m_{BRF}}{|s_{BRF} \times m_{BRF}|} \\
t_{3_{BRF}} &= t_{1_{BRF}} \times t_{2_{BRF}} \\
t_{1_{ORF}} &= s_{ORF} \\
t_{2_{ORF}} &= \frac{s_{ORF} \times m_{ORF}}{|s_{ORF} \times m_{ORF}|} \\
t_{3_{ORF}} &= t_{1_{ORF}} \times t_{2_{ORF}}
\end{aligned}$$

Two rotation matrices can be constructed bringing from the triad **TRD** to **BRF** and **ORF**:

$$\begin{aligned}
M_{B \leftarrow T} &= [t_{1_{BRF}}, t_{2_{BRF}}, t_{3_{BRF}}] \\
M_{O \leftarrow T} &= [t_{1_{ORF}}, t_{2_{ORF}}, t_{3_{ORF}}]
\end{aligned} \tag{4.2}$$

Then the attitude matrix $M_{B \leftarrow O}$ can be easily calculated:

$$M_{B \leftarrow O} = M_{B \leftarrow T} [M_{O \leftarrow T}]^T \tag{4.3}$$

Having defined the sequence of Euler angles rotations to move from the **ORF** to the **BRF**, the three attitude angles can be easily derived (for example inverting the trigonometric expressions in Eq. 2.12 or using the simple quaternions' inversion formulas described in Sect. 2.3.1).

If we assume now, that measurement is affected by random Gaussian error, the expression of the attitude error covariance matrix can be computed and shows that it is inversely proportional to the angle between the Sun and magnetic field vectors also called co-linearity angle. In general, orbit transient phases where the co-linearity is low or null may exist. In such periods of time this algorithm cannot be used and it is customary to propagate the attitude with a gyroscope.

The expression of the attitude error covariance is found to be (see [8, 9]):

$$\begin{aligned}
P &= \sigma_S^2 I + \frac{1}{||s_{BRF} \times m_{BRF}||^2} [(\sigma_B^2 - \sigma_S^2) s_{BRF} s_{BRF}^T \\
&\quad + \sigma_S^2 (s_{BRF}^T m_{BRF}) (s_{BRF} m_{BRF}^T + m_{BRF} s_{BRF}^T)]
\end{aligned} \tag{4.4}$$

$\sigma_{S_{ref}}$ = Sun reference half cone error covariance

$\sigma_{S_{meas}}$ = Sun measured half cone error covariance

$\sigma_{B_{ref}}$ = B field reference half cone error covariance

$\sigma_{B_{meas}}$ = B field measured half cone error covariance

$$\begin{aligned}
\sigma_S^2 &= (\sigma_{S_{ref}})^2 + (\sigma_{S_{meas}})^2 \\
\sigma_B^2 &= (\sigma_{B_{ref}})^2 + (\sigma_{B_{meas}})^2
\end{aligned} \tag{4.5}$$

In case of more reference and observation vectors, a better attitude estimate can be achieved using the *Quest* algorithm that finds an optimal weighted overlap of measurement and references (see [10]).

For a coarse attitude estimate using Sun sensor and magnetometer measurement the *Triad* algorithm is a good compromise between the computational effort and the achieved accuracy.

4.3.5.2 Fine Attitude Determination Algorithm

The fine attitude determination algorithm is based on gyro and star tracker measurement. The gyro rate is used to propagate the attitude kinematic equation (2.11); the residual between star tracker measurement and propagated attitude estimate, properly weighted by filter gains, is added to the gyro measured rate to correct the attitude prediction and to estimate the gyro rate drift.

The attitude dynamics in terms of quaternions is described by the kinematic equation (2.11):

$$\dot{q} = \frac{1}{2}(0, \omega) \otimes q \quad (4.6)$$

where q is the attitude quaternion that describes the spacecraft attitude orientation providing the transformation matrix $M_{B \leftrightarrow E}$ from **ECI** to **BRF** using Eq. 2.9, while $\omega = \omega_{BE,B}$ is the spacecraft angular rate in **BRF** components.

The Star tracker sensor will provide a noisy attitude quaternion measurement, the noise being higher in the direction of the sensor bore-sight. This noise will produce noisy dynamics of the controlled attitude and poor pointing performances. The sensor error is not actually made up only of random noise: important bias and low frequency error components also affect the measurement quality.

However, it is customary to calculate the attitude determination algorithms using a random noise hypothesis because this method produces good results and simplifies the calculations of the filter gains.

It is also possible to treat the low frequency errors by introducing a suitable dynamic model of these errors, though this approach will not be presented here.

The purpose of the attitude determination filter is to fuse the measurements from other star trackers and a gyro in order to minimize the noise of the final estimated quaternion.

Let us indicate the measured quaternion of the i th star tracker q_i and $q_{n,i}$ the error quaternion of i -th star tracker, subscript n indicates that this quaternion depends only on the measurement noise. The true spacecraft attitude can be obtained by multiplying the small error quaternion with the star tracker measured attitude quaternion (see 2.10):

$$q = q_{n,i} \otimes q_i \quad (4.7)$$

Neglecting the bias and low frequency error components, the error quaternion $q_{n,i}$ is supposed to be due only to random zero mean Gaussian white noise. It can be

assumed that $q_{n,i}$ represents a near identity transformation, so that it is possible to consider the scalar part q_0 equal to one and the vector part $\|\mathbf{q}_{n,i}\| \ll 1$ so that, to the first order, the norm of the quaternion is still unitary: $q_{n,i} \approx (1, \mathbf{q}_{n,i})$. This is how small rotations are represented in the quaternion theory for linearization purposes.

Given \mathbf{n}_i the i th sensor noise in the star tracker reference frame, $\Theta_i = E[\mathbf{n}_i \mathbf{n}_i^T]$ the star tracker covariance matrix (the matrix containing the PSD of the noise in the star tracker reference frame, for the definition of PSD see Sect. 5.3) and $M_{B \leftarrow S_i}$ the transfer matrix describing the orientation of the i th star tracker reference frame with respect to the spacecraft BRF, the error quaternion $\mathbf{q}_{n,i} = M_{B \leftarrow S_i} \mathbf{n}_i$ PSD is obtained as follows:

$$E[\mathbf{q}_{n,i} \mathbf{q}_{n,i}^T] = E[M_{B \leftarrow S_i} \mathbf{n}_i \mathbf{n}_i^T M_{B \leftarrow S_i}^T] = M_{B \leftarrow S_i} \Theta_i M_{B \leftarrow S_i}^T \quad (4.8)$$

It can be assumed that the spacecraft's angular rate is related to the gyro ω_g measurement according to the following equation:

$$\begin{cases} \omega = \omega_g + \mathbf{b} + \mathbf{n}_g \\ \dot{\mathbf{b}} = 0 \end{cases}$$

where:

ω is the true spacecraft rate referred to the body fixed reference frame

ω_g is the gyro measured spacecraft rate already converted to body reference frame

\mathbf{b} is the gyro drift supposed to be almost constant in time ($\dot{\mathbf{b}} = 0$)

\mathbf{n}_g is the gyro random noise modeled as zero mean Gaussian noise

Let us define the state of our process given by $\begin{pmatrix} q \\ b \end{pmatrix}$ and its estimate by $\begin{pmatrix} \hat{q} \\ \hat{b} \end{pmatrix}$

where \hat{q} is the attitude quaternion estimate and \hat{b} is the gyro drift estimate.

As shown in Sect. 5.3, the state estimation filter copies the state dynamics equations augmented by a forcing term which is linear in the error between measurements and estimate. Under certain assumptions the estimated state converges to the true state. We will follow this approach. Let us now indicate q_e the small error quaternion estimate so that:

$$q = q_e \otimes \hat{q} \quad (4.9)$$

The error quaternion estimate q_e is supposed to be very small so that it is possible to consider the scalar part almost equal to one $q_e \approx (1, \mathbf{q}_e)$.

Combining Eqs. 4.7 and 4.9 it is possible to calculate the residual quaternion between the star tracker measurement quaternion and the attitude quaternion estimate. Let us define $q_{r,i}$ the residual quaternion:

$$q_{r,i} = q_i \otimes \hat{q}^{-1} \quad (4.10)$$

Using the quaternion multiplication rule defined in Sect. 2.10 we have:

$$q_{r,i} = q_{n,i}^{-1} \otimes q \otimes \hat{q}^{-1} = q_{n,i}^{-1} \otimes q \otimes q^{-1} \otimes q_e = q_{n,i}^{-1} \otimes q_e.$$

Neglecting the second order terms $O(\mathbf{q}_{n,i}^T \mathbf{q}_e)$ the i th star tracker residual can be written as:

$$q_{r,i} = (1, \mathbf{q}_e - \mathbf{q}_{n,i}) \quad (4.11)$$

Considering that the residual quaternion is very small, defining $\mathbf{e} = (e_1, e_2, e_3)$ the angular residual error between the star tracker measurement and the quaternion estimate, it is possible to assume the angular residual error equal to twice the quaternion's vector components:

$$e_i = 2\mathbf{q}_{r,i} = 2(\mathbf{q}_e - \mathbf{q}_{n,i}) \quad (4.12)$$

The following equations can now be used for the state prediction:

$$\begin{aligned} \dot{\hat{q}} &= \frac{1}{2}(0, \hat{\omega}) \otimes \hat{q} \\ \dot{\hat{b}} &= \sum_{i=1}^n K_{b,i} \mathbf{e}_i \\ \hat{\omega} &= \omega_g + \hat{\mathbf{b}} + \sum_{i=1}^n K_{m,i} \mathbf{e}_i \\ \mathbf{e}_i &= 2\mathbf{q}_{r,i} = 2(q_i \otimes \hat{q}^{-1})|_{1,2,3} \end{aligned} \quad (4.13)$$

The $K_{b,i}$ and $K_{m,i}$ are the filter gains matrices. They represent the weights given to the measurement error. In order to optimize the gains, the dynamics of the error estimate is derived.

From Eq. 4.9 the estimate error quaternion can be derived:

$$q_e = q \otimes \hat{q}^{-1} \quad (4.14)$$

Differentiating Eq. 4.14 we get:

$$\dot{q}_e = \dot{q} \otimes \hat{q}^{-1} + q \otimes \frac{d}{dt} \hat{q}^{-1} \quad (4.15)$$

The first addendum can be computed using Eq. 2.11, the second using:

$$\frac{d}{dt} (\hat{q} \otimes \hat{q}^{-1}) = \frac{d}{dt} \hat{q} \otimes \hat{q}^{-1} + \hat{q} \otimes \frac{d}{dt} \hat{q}^{-1} = 0 \quad (4.16)$$

From which it is easy to derive using the fist of Eq. 4.13:

$$\frac{d}{dt} \hat{q}^{-1} = -\frac{1}{2} \hat{q}^{-1} \otimes (0, \hat{\omega}) \quad (4.17)$$

Therefore the error dynamics equation becomes:

$$\dot{q}_e = \frac{1}{2}(0, \omega) \otimes q_e + \frac{1}{2}q_e \otimes (0, -\hat{\omega}) \quad (4.18)$$

Assuming that:

$$\omega - \hat{\omega} = \delta\omega \quad (4.19)$$

$$q_e = (1, \mathbf{q}_e) \quad (4.20)$$

We get:

$$\begin{aligned} \frac{1}{2}((0, \omega) \otimes q_e + q_e \otimes (0, -\omega)) &= -(0, \omega \times q_e) \\ \frac{1}{2}q_e \otimes (0, \delta\omega) &\approx (0, \delta\omega) \end{aligned} \quad (4.21)$$

Equation 4.18 written in quaternion vector component becomes:

$$\dot{\mathbf{q}}_e = -\omega \times \mathbf{q}_e + \frac{1}{2}\delta\omega \quad (4.22)$$

Considering also:

$$\delta\mathbf{b} = \mathbf{b} - \hat{\mathbf{b}} \implies \dot{\delta\mathbf{b}} = -\dot{\hat{\mathbf{b}}} \quad (4.23)$$

$$\omega \times \mathbf{q}_e = skew(\omega)\mathbf{q}_e \quad (4.24)$$

$$skew(\omega) = \begin{bmatrix} 0 & -\omega_3 & \omega_2 \\ \omega_3 & 0 & -\omega_1 \\ -\omega_2 & \omega_1 & 0 \end{bmatrix} \quad (4.25)$$

we are in condition to write the following error dynamics equation:

$$\begin{cases} \dot{\mathbf{q}}_e = -skew(\omega)\mathbf{q}_e - (K_{m,1} + K_{m,2})\mathbf{q}_e + \frac{1}{2}\delta\mathbf{b} + \frac{1}{2}\mathbf{n}_g + K_{m,1}\mathbf{q}_{n,1} + K_{m,2}\mathbf{q}_{n,2} \\ \dot{\delta\mathbf{b}} = -(K_{b,1} + K_{b,2})\mathbf{q}_e + K_{n,1}\mathbf{q}_{n,1} + K_{b,2}\mathbf{q}_{n,2} \end{cases} \quad (4.26)$$

Assuming that $skew(\omega) \ll (K_{m,1} + K_{m,2})$ Eq. 4.26 can be simplified and in matrix form becomes:

$$\begin{pmatrix} \dot{\mathbf{q}}_e \\ \dot{\delta\mathbf{b}} \end{pmatrix} = \begin{bmatrix} -(K_{m,1} + K_{m,2}) & \frac{1}{2} \\ -(K_{b,1} + K_{b,2}) & 0 \end{bmatrix} \begin{pmatrix} \mathbf{q}_e \\ \delta\mathbf{b} \end{pmatrix} + \begin{bmatrix} K_{m,1} & K_{m,2} \\ K_{b,1} & K_{b,2} \end{bmatrix} \begin{pmatrix} \mathbf{q}_{n,1} \\ \mathbf{q}_{n,2} \end{pmatrix} + \frac{1}{2} \begin{bmatrix} I \\ 0 \end{bmatrix} \mathbf{n}_g \quad (4.27)$$

In the case of only one star tracker available, the system of equations becomes:

$$\begin{pmatrix} \dot{\mathbf{q}}_e \\ \dot{\delta\mathbf{b}} \end{pmatrix} = \begin{bmatrix} -K_{m,1} & \frac{1}{2} \\ -K_{b,1} & 0 \end{bmatrix} \begin{pmatrix} \mathbf{q}_e \\ \delta\mathbf{b} \end{pmatrix} + \begin{bmatrix} K_{m,1} \\ K_{b,1} \end{bmatrix} \mathbf{q}_{n,1} + \frac{1}{2} \begin{bmatrix} I \\ 0 \end{bmatrix} \mathbf{n}_g \quad (4.28)$$

We choose to select diagonal gain matrices in order to simplify the design and uncouple the body measurement axes. The convergence of the error is determined by the roots of the polynomials which identify the eigenvalues of Eq. 4.28, if k_m , k_b , are the generic diagonal element of the $K_{m,1}$, $K_{b,1}$ matrices, the polynomial for the corresponding axis is:

$$s^2 + k_m s + \frac{1}{2}k_b \quad (4.29)$$

so that, being ω_f and ζ_f the filter angular frequency and damping, it follows that

$$\begin{cases} k_m = 2\zeta_f \omega_f \\ k_b = 2\omega_f^2 \end{cases} \quad (4.30)$$

The attitude filter is a second order low pass filter for each measurement axis, where k_m and k_b determine the damping coefficient and the natural frequency. In this case the gain synthesis can be directly carried out by setting the filter poles in the frequency domain.

In case of two star trackers from Eq. 4.27 we derive the same Eq. 4.29 for the eigenvalues, here k_m , k_b , are the generic diagonal element of the $K_{m,1} + K_{m,2}$, $K_{b,1} + K_{b,2}$ matrices. In addition, the steady state error effect due to the star tracker noise can be easily derived from the same equation:

$$\delta \dot{\hat{b}} \rightarrow 0 \implies q_e \rightarrow (K_{b,1} + K_{b,2})^{-1}(K_{b,1}q_{n,1} + K_{b,2}q_{n,2}) \quad (4.31)$$

Assuming that the star tracker error source is a stationary random process, after the filter convergence, the error covariance matrix depends only on the $K_{b,1}$, $K_{b,2}$ filter gains:

$$E[q_e q_e^T] = (K_{b,1} + K_{b,2})^{-1}(K_{b,1}E[q_{n,1}q_{n,1}^T]K_{b,1} + K_{b,2}E[q_{n,2}q_{n,2}^T]K_{b,2})(K_{b,1}^T + K_{b,2}^T)^{-1} \quad (4.32)$$

For spacecraft rates verifying $skew(\omega) \ll (K_{m,1} + K_{m,2})$, the system gains can be synthesized with an optimization method that minimizes the trace of the error covariance matrix:

$$K_{b,i} = argmin(tr(E[q_e q_e^T])), \quad i = 1, 2 \quad (4.33)$$

under constraints on the $K_{m,i}$, $K_{b,i}$ gains, derived taking into account that a reduction of the filter frequency produces a better error smoothness at steady state, but also an increase of the gyro noise effect.

| | AOCS MODES REQUIRED HW | | | | | | | |
|--------|------------------------|----|-----|-----|------|-----|-----|-----|
| | MGT | RW | RCT | FSS | GYRO | MGM | GPS | STT |
| SAM-EM | + | X | - | X | X | + | | |
| NPM | + | X | | | X | | + | X |
| OCM | + | X | - | | X | | + | X |
| SHM | + | X | | X | | + | | |

(+) HW used only in LEO ; (-) HW used only in GEO ; (x) common HW

Fig. 4.6 AOCS operational modes HW usage

4.4 AOCS Mode Algorithms

As previously mentioned, the design of the *multi-mission* AOCS includes the following operational modes:

- Sun acquisition mode-emergency mode (SAM-EM);
- normal pointing mode (NPM);
- orbit control mode (OCM).
- safe hold mode (SHM) specific for LEO-SSO missions;

Figure 4.6 specifies the hardware used in each AOCS operational mode.

4.4.1 Sun Acquisition Mode-Emergency Mode

The Sun acquisition mode-emergency mode (SAM-EM) is used to perform a robust and fast acquisition of the Sun pointing attitude.

The SAM-EM may be used in different S/C platform configurations and is applied in some nominal phases (i.e. to point solar arrays towards the Sun in order to reload the batteries) as well as in contingency scenarios. The emergency mode is made up of the following submodes:

- rate damping;
- Sun search;
- coarse Sun pointing;
- fine Sun pointing;
- eclipse.

The SAM-EM may be entered by ground TC or at any time during the mission according to FDIR logic. The SAM-EM mode is able to guarantee the stability and performance requirements in any of the nominal S/C configurations (from stowed to fully deployed).

| SAM-EM Submodes | MGT | RW | RCT | FSS | GYRO | MGM | GPS | STT |
|---------------------|-----|----|-----|-----|------|-----|-----|-----|
| Rate Damping | + | x | - | x | x | + | | |
| Sun Search | + | x | - | x | x | + | | |
| Coarse Sun Pointing | + | x | - | x | x | + | | |
| Fine Sun pointing | + | x | - | x | x | + | | |
| Eclipse | + | x | - | | x | + | | |

(+) HW used only in LEO ; (-) HW used only in GEO ; (x) common HW

Fig. 4.7 SAM-EM submodes

The SAM-EM provides an attitude, controlled either around all three attitude angles (typical in LEO), or around two attitude angles orthogonal to the Sun direction and in rate around the Sun direction (typical in GEO or GTO). The reference attitude is configurable—in a given set defined by the Sun sensors field of view (see Chap. 9)—through the ground TCs.

In LEO, with three axes control, a coarse attitude estimation algorithm like the *Triad* is required (see Sect. 4.3.5.1). To cope with this need the SAM-EM design uses not only the magnetometer (MGM) and the FSS (fine Sun sensor) as AOCS sensors but also a coarse orbital propagator (COD) and a magnetic field model that allow to estimate the magnetic field in **ORF** necessary for the *Triad* algorithm (see Sect. 4.3.5.1).

Figure 4.7 lists for each submode AOCS hardware used in the control loop.

4.4.1.1 Rate Damping

The rate damping submode (Fig. 4.8) is a derivative loop with a zero angular rate reference. Its goal is to slow down the S/C rates and to take the system to an inertial attitude from which the Sun search phase can be safely and successfully started. The rate damping phase reduces the spacecraft angular rate below a pre-defined threshold on each axis. The SAM-EM is able to quickly despin the spacecraft if the stored angular momentum does not exceed a predefined value compatible with the RW Assembly overall momentum capability.

The primary sensor used during this phase is the gyro package and the actuators used are the RWs.

The exit condition is the achievement of adequately low rates on all three axes.

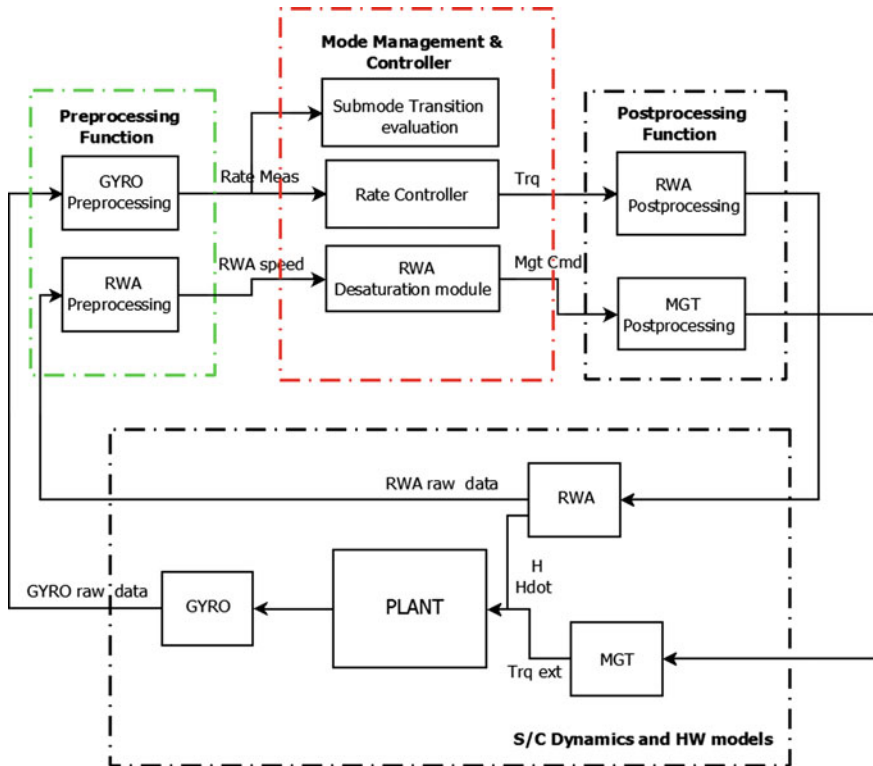


Fig. 4.8 EM rate dumping functional flow

4.4.1.2 Sun Search

The Sun search submode is entered after successful completion of the rate damping phase. Its goal is to maneuver the spacecraft so to perform a rotation about an axis fixed in BRF to bring the Sun in the FOV of a Sun sensor. The on-board collocation and orientation of the FSSs (fine Sun sensors) must provide a full coverage of the space after a 360 deg. rotation around this fixed axis, such that the Sun occurrence in one of the FSS FOV is guaranteed. When said condition is achieved (i.e. Sun in FOV), the coarse Sun pointing submode is automatically entered.

The primary sensor used during this phase is the gyro package and the actuators are the RWs while the Sun sensors are only used to trigger the Sun's presence.

At submode entrance, if the Sun is already present in the FSS field of view, the sense of rotation is chosen in order to move towards the Sun. In this case the Sun search will last only the time needed to confirm the Sun's presence.

The Sun search functional flow diagram is shown in Fig. 4.9, where it is possible to see that the core structure of the controller is a rate controller which commands the rotation rate desired to have the Sun entering in the FSS field of view.

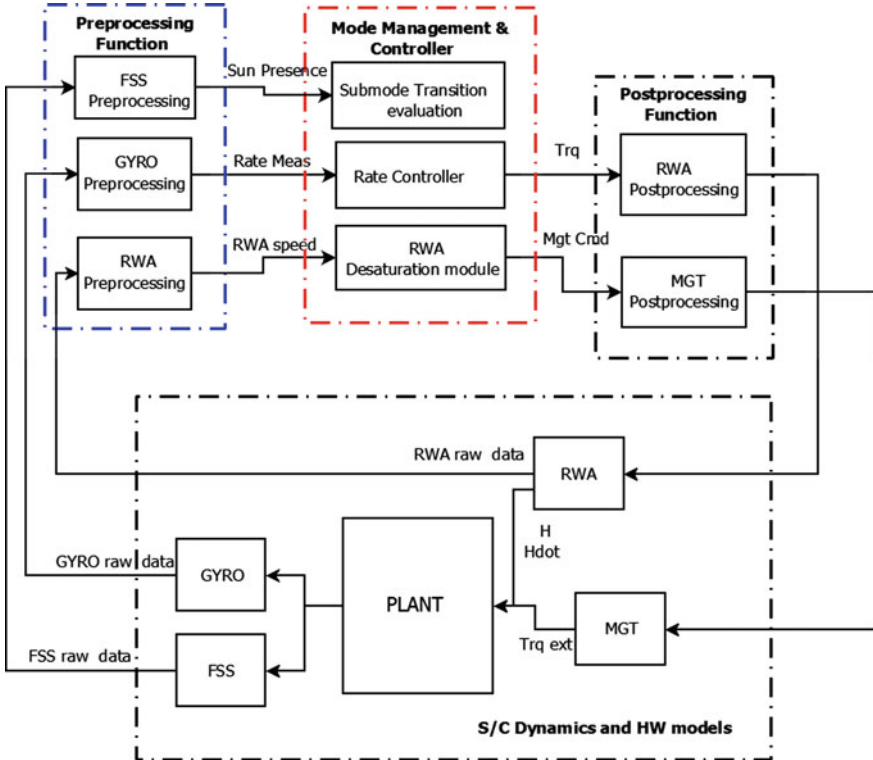


Fig. 4.9 EM sun search functional flow

4.4.1.3 Coarse Sun Pointing

The coarse Sun pointing (CSP) submode is entered after the accomplishment of the Sun search submode. This submode has two specific implementations: one applicable to LEO mission and one applicable to GEO mission.

4.4.1.4 Coarse Sun Pointing in LEO

It consists of a sequence of three large orthogonal rotations, realized for example according to the Euler angles rotation sequence 1-3-2 (see [6]). At the start of the sequence an estimate of the satellite attitude errors with respect to a desired attitude is obtained using a coarse attitude estimation algorithm that combines, in a *Triad-like* algorithm, the low accuracy Sun sensor and magnetometer measurement with the related reference provided by the available orbital propagator. After a sequence of roll, yaw and pitch rotations is defined to reach the desired Sun pointing attitude.

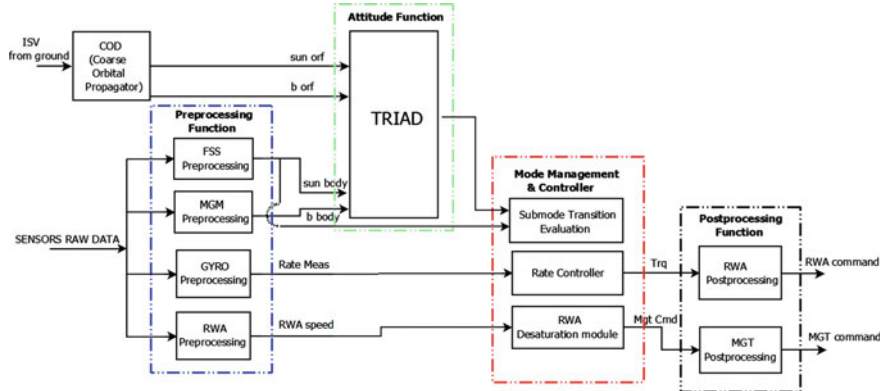


Fig. 4.10 Coarse sun pointing functional flow in LEO

During each rotation of the sequence, the control error is provided by the gyro measured rate so that two axes are kept at null rate and in the third the desired angle of rotation is integrated with the gyro rate until the desired rotation is obtained.

The combination of the first two maneuvers will bring the Sun in the X_{BRF}/Z_{BRF} plane. At this point it is necessary only to implement the pitch maneuver.

In case of no eclipse, as soon as the three attitude errors have been reduced, the transition to fine Sun pointing submode will be performed. In Fig. 4.10 the coarse Sun pointing functional flow is shown.

4.4.1.5 Coarse Sun Pointing in GEO

In GEO AOCS we typically do not have a coarse three axis measurement (because the magnetic field is too low), therefore the acquisition cannot be based on a full three axis maneuver computation.²

The main sensors used in CSP submode in GEO are gyro and FSS, while in LEO also the MGM was used to have a three axis attitude determination.

In GEO a different algorithm based on a two axis control instead of a three axis control can be used. The error signal is computed as the cross vector product between the Sun unit vector measured **BRF** and the target Sun unit vector in the **BRF** attitude. The target Sun unit vector in body axis is typically selected in order to maximize the solar array power generation. This error signal is then projected in the body reference frame and it is used as position error while the gyro measurement is used as rate error (i.e. the controller is a PD control loop).

The Sun acquisition in GEO is split in two parts: coarse acquisition and fine acquisition. These two phases use the same control loop structure, but with differ-

²The use of star trackers to perform Sun Pointing modes with three axes attitude measurement has been proposed and is becoming a possibility considering the good reliability of current STTs. However the question is much debated considering that most designers prefer to use different sensors for contingency (the SAM-EM is also a contingency mode) and nominal modes.

ent gains. This choice provides a smooth and gradual acquisition process without undesired transients. In fine Sun pointing, ground may command angular bias values and rate bias values around the Sun line if they are required (e.g. to have gyroscopic stiffness around that axis).

4.4.1.6 Fine Sun Pointing

The fine Sun pointing submode is entered after the successful completion of the coarse Sun pointing and guarantees that the attitude errors are lower than a pre-defined threshold.

This submode consists of a proportional derivative loop which is fed-in by attitude errors signal (proportional channel) and by the gyroscope measurements (derivative channel).

The sensors used during this phase are the gyro, the FSS and the MGM (only in LEO mission).

In LEO missions using the MGM, we can implement a three axis position control, without the MGM, like in most GEO missions, the control around the Sun direction is merely derivative and may allow for a slow drift of the satellite attitude.

The main actuators in the loop are the RWs. The MGMs and MGTs are used in LEO to desaturate the reaction wheels (RWs) stored angular momentum while the RCTs are used in GEO to desaturate the reaction wheels (RWs) stored angular momentum.

The emergency fine Sun pointing functional flow (for LEO mission) is shown in Fig. 4.11.

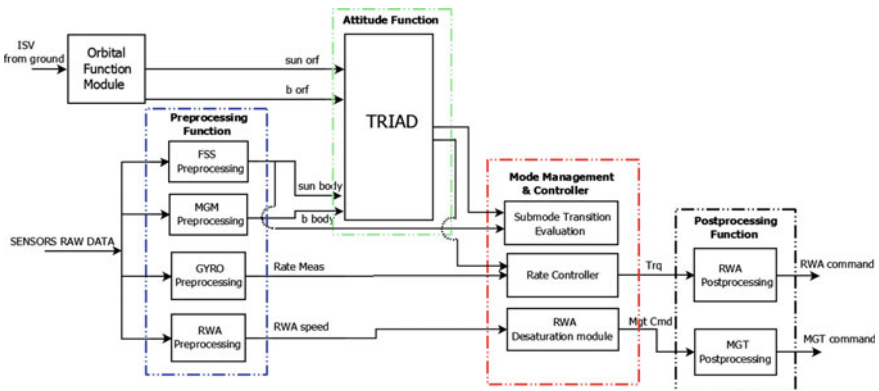


Fig. 4.11 EM fine sun pointing functional flow in LEO

4.4.1.7 Eclipse

The eclipse submode is automatically entered during the eclipse periods from Sun search, coarse Sun pointing and fine Sun pointing submodes. It consists in a derivative loop (see Fig. 4.12). The eclipse can be tackled in different ways depending on the orbital conditions (LEO or GEO) and the entry submode.

Specifically:

1. When the previous submode was the Sun search, the loop is fed-in with a null angular rate reference. This is done to resume the Sun search exactly from the point in which it was interrupted.
2. When the eclipse is entered from a fine Sun pointing or coarse Sun pointing submode in the LEO, the loop is fed-in with the orbital rate along the direction normal to the orbital plane.

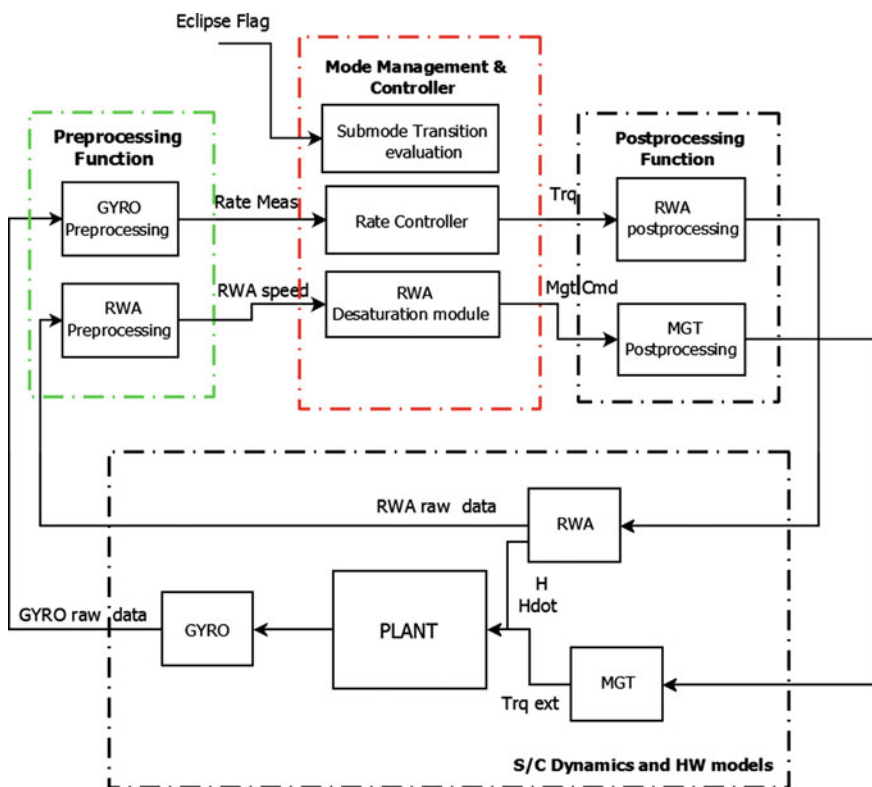


Fig. 4.12 EM eclipse functional flow

3. When the eclipse is entered from a fine Sun pointing or coarse Sun pointing submode in the GEO, a bias or null angular rate around the Sun line is commanded. This small rate bias provides some gyroscopic stiffness, so that at the end of the eclipse the Sun is expected to reappear close to its reference. At eclipse exit the rate damping submode, as well as the following Sun search and coarse Sun pointing submodes, should find all forward conditions verified, and should last only few seconds, before the new transition into fine Sun pointing.

For attitude control the sensor used during this phase is the gyro package, and the actuators are the RWs. The MGM and MGT are also used to desaturate the RWs' stored angular momentum in LEO mission, RCT are used in GEO with the same scope. The exit from the eclipse is triggered by the eclipse state provided by the on-board propagator or by a timer set by ground.

4.4.1.8 SAM-EM Control Loop

4.4.1.9 Rate Control Loop Structure

The SAM-EM rate control loop is a pure proportional rate controller. This control loop is used in rate damping, Sun search and coarse Sun pointing submode, to implement open loop S/C rotations.

The proposed control structure is shown in Fig. 4.13 where $H_p(s)$ is the plant, $H_g(s)$ is the gyro pre-filtering and $K_d H_c(s)$ is the controller.

Where:

$$H_c(s) = K_f \frac{1 + \tau_f s}{s^2 + 2\zeta_f \omega_f s + \omega_f^2} \quad (4.34)$$

$$H_g(s) = \frac{1}{1 + \tau_g s} \quad (4.35)$$

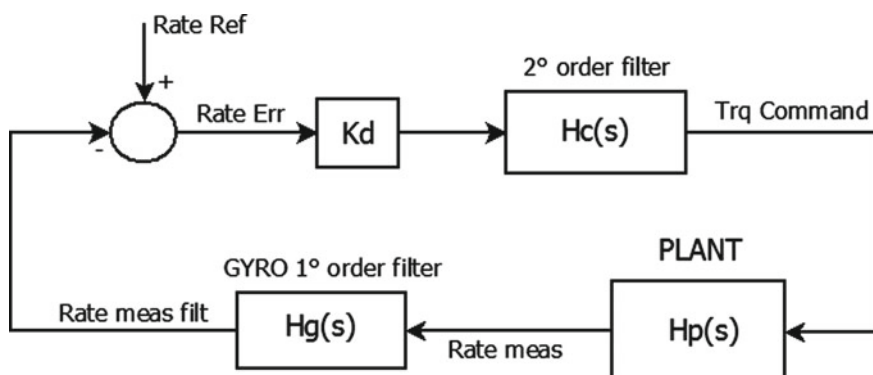


Fig. 4.13 EM rate control loop

The Plant is made up of a satellite with flexible appendages (e.g. solar array and antennas). The complete set of linear differential equations that can be used to describe the dynamics of a body with flexible appendages can be found in Chap. 3 Eqs. 3.136 and 3.137.

In a more general form, the plant is a multi Input multi Output (MIMO) system that implies that the control design has to be approached with control techniques (e.g. LQG/LQR, H_∞ , ...) suitable for this class of dynamic systems (see Sect. 6.3).

However, in many cases like the one we consider here, the plant has a highly diagonally dominant matrix of inertia and modal participation factors aligned to the principal axes. The plant can be assumed as three separate Single Input Single Output (SISO) systems obtained through the transfer function built around the diagonal elements of the matrix of inertia. Thus, it is possible to use a more simple control technique in frequency domain or time domain (e.g. poles place, root locus, PID controller synthesis, phase-lag and phase lead compensator...) to synthesize the controller (many text are available to study these basic techniques see among the others [11–13]).

Following this consideration, we recall that Eq. 3.136, bring to the following plant transfer function:

$$\delta\phi = (I_G - s^2 \sum_{k=1 \dots N_f} \frac{S_G^k S_G^{kT}}{s^2 + \Omega_k^2})^{-1} \frac{u}{s^2} \quad (4.36)$$

where $u = \delta c_c - \delta \dot{h}_w - [\delta\dot{\phi}, \bar{h}_w]$ is the control torque. In this case we assume $\delta c_c = 0$, and $\bar{h}_w = 0$, so that $u = -\delta \dot{h}_w$.

If we specialize Eq. 4.36 to a single axis transfer function $H_p(s)$ from the control torque to the attitude angle output, considering only a two iso-frequency dominant flexible modes composed of two symmetric appendages (see also [14]), we obtain:

$$H_p(s) = \frac{s^2 + \Omega_1^2}{J s^2 ((1 - 2\delta^2/J)s^2 + \Omega_1^2)}$$

where J is the diagonal component of the matrix I_G in the selected axis, ($\Omega_1 = \Omega_2$) is the cantilevered angular frequency of the first dominant flexible mode while the pole ($\frac{\Omega_1}{\sqrt{1-2\delta^2/J}}$) is the free-free frequency of this flexible mode. The factor δ is the participation factor, corresponding to the square root of the diagonal component of the matrix $S_G^{-1} S_G^{1T} = S_G^{-2} S_G^{2T}$ on the selected axis. It is counted twice because we are assuming to have two identical symmetric appendages.

In the proposed AOCS architecture, we have direct access to the rate measurement using a gyro as a rate sensor. The filter $H_g(s)$ is introduced as a pre-filter to reduce the output noise of the rate sensor. To simplify the control design and gain selection,

the cut-off frequency of the gyro pre-processing filter has to be selected at least one decade higher than the control bandwidth in order not to limit the bandwidth of the controller.

Figure 4.13 shows a second order filter $H_c(s)$ introduced to filter the flexible appendages (i.e. solar arrays). To design this filter we can use different techniques mainly related to the level of amplitude reduction and phase shaping needed at a predefined frequency. A possible structure of this filter is shown in Eq. 4.34.

Due to the fact that in this mode a very large bandwidth is not necessary, the controller is simply a gain Kd that has been tuned for all S/C configurations (i.e. in stowed and deployed configuration). Its value is selected in order to obtain the desired static error in the rate loop.

This simple solution is enough to achieve the desired bandwidth with sufficient margins both for the phase and amplitude without using a more complicated structure like the phase-led/phase-lag compensator [11, 12].

A typical bode diagram for this type of control loop chain is shown in Fig. 4.14.

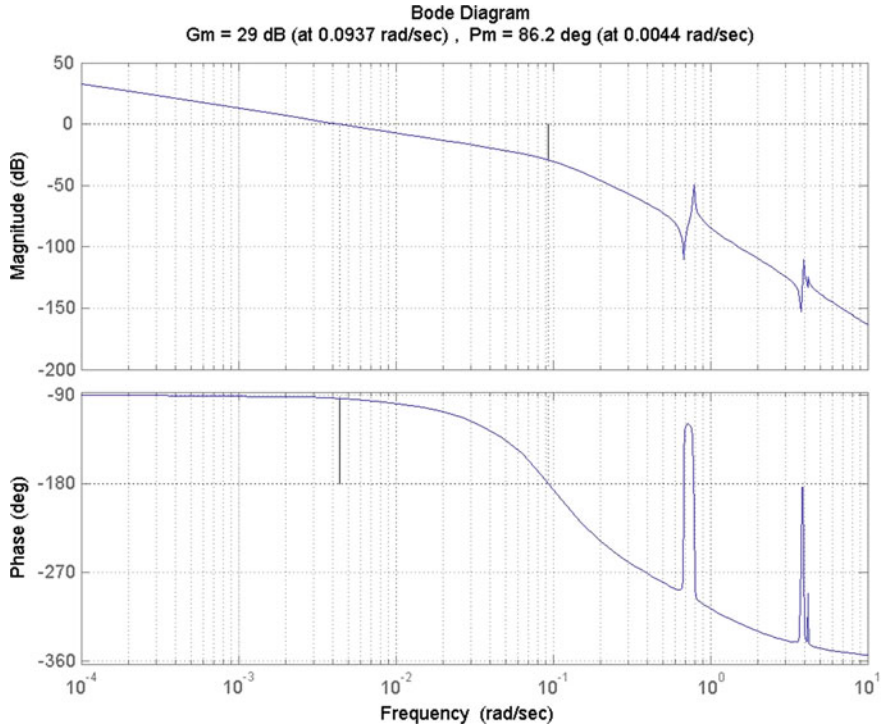


Fig. 4.14 Bode open loop chain—rate control loop

In this picture, it is possible to recognize that the control loop has a derivative action up to the selected bandwidth (0.004 rad/s), high gain margin and phase margin and it has a strong gain reduction (up to 50 db) on the peak of the first frequency of the solar array.

4.4.1.10 Rate and Position Control Loop Design

The rate and position control loop is a proportional-derivative (PD) controller used in the Sun pointing submode to perform three axis attitude control. The plant structure, pre-filtering and flexible mode filter presented in the previous chapter can be reused for this new control chain.

Figure 4.15 shows a rate and position control loop structure.
where:

$$H_c(s) = K_f \frac{1 + \tau_f s}{s^2 + 2\zeta_f \omega_f s + \omega_f^2} \quad (4.37)$$

$$H_g(s) = \frac{1}{1 + \tau_g s} \quad (4.38)$$

The main difference between this control structure and the rate control loop is in the selection of a PD controller instead of only derivative controller. The K_p and K_d gain selection can be carried out using different techniques like the Ziegler-Nichols method (see [12]) or an equivalent approach for the design of a phase-lead compensator (see [11]).

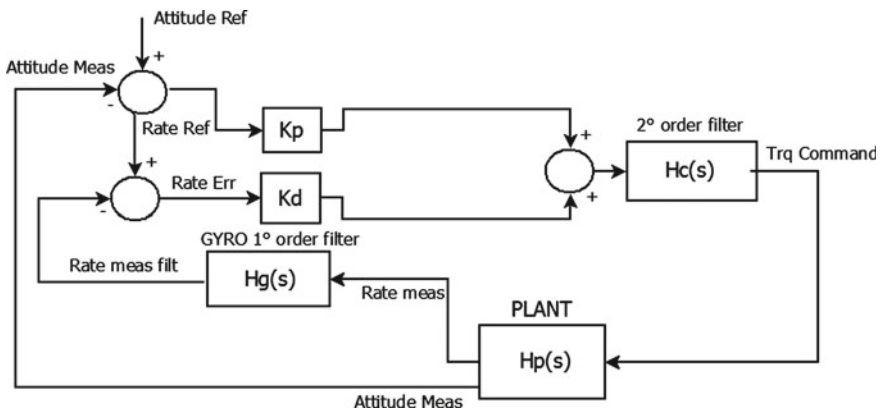


Fig. 4.15 EM rate and position control loop

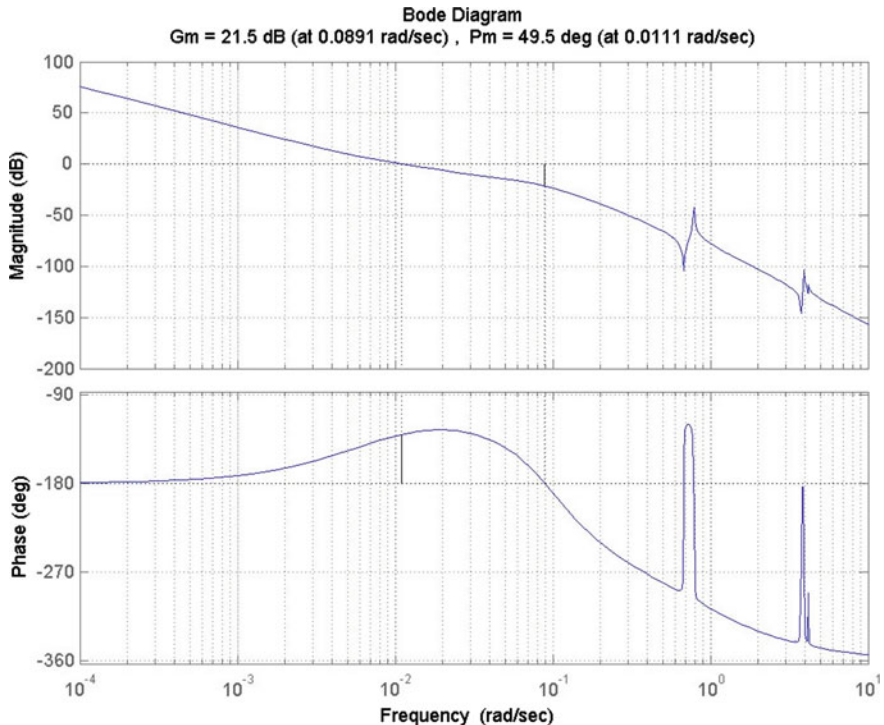


Fig. 4.16 Bode open loop chain—position rate control loop

All the control parameters have to be selected according to a design process able to guarantee the desired performance and appropriate stability margin and gain margin that ensure a robustness with respect to gain loop reduction or time delay in the loop.

The open loop bode diagram of the rate and position loop is shown in Fig. 4.16.

4.4.1.11 SAM-EM Simulation

This section shows some simulation results of SAM-EM obtained using the design solution presented in the previous sections. In particular, the simulation results are related to a S/C in fully deployed condition (i.e. all appendages deployed) with a not-null initial attitude angle and angular rates during a Summer Solstice in a SSO orbit.

The spacecraft data used for the simulations are shown in the following tables.

The inertia tensor of the fully integrated satellite including the appendages is shown in Fig. 4.17.

The appendages considered are two identical solar array wings (SAW1 and SAW2), connected to the main body in two hinges positioned in:

$$r_{SAW1} = (0.6829, 0.7908, 1.2711)^T [m], \text{ and } r_{SAW2} = (-0.6829, -0.7908, 1.2711)^T [m].$$

| Inertia tensor is a 3x3 matrix [kgm^2] w.r.t a body fixed frame centred in the S/C COG parallel to the mechanical build reference. [kgm^2] | | | | | | |
|---|----------|----------|----------|----------|----------|----------|
| DESCRIPTION | I_{xx} | I_{yy} | I_{zz} | I_{xy} | I_{xz} | I_{yz} |
| DEPLOYED Conf. | 3467.0 | 17193.0 | 14566.0 | -512.0 | 56.3 | 35.3 |

Fig. 4.17 Spacecraft inertia tensor

| Diagonal component [Hz] | Minimal | Tolerance |
|-------------------------|---------|-----------|
| 1° Out of plane | 0.1039 | 10% |
| 1° In plane | 0.5356 | 10% |
| 2° Out of plane | 0.6635 | 10% |
| 1° Torsional | 0.8259 | 10% |

Fig. 4.18 Modal natural frequencies of the SAW in deployed configuration

| SAW modal damping coefficients | | |
|--|--|-------|
| The Solar Panel properties are reported in the fully deployed configuration. | | |
| 1° Out of plane | | 0.003 |
| 1° In plane | | 0.003 |
| 2° Out of plane | | 0.003 |
| 1° Torsional | | 0.003 |

Fig. 4.19 Modal damping coefficients of the SAW in deployed configuration

| SAW Modal Rotation Coupling Factors | | | |
|---|---------------|---------------|---------------|
| The Solar Panel modal rotation coupling factors are reported in the fully deployed configuration. | | | |
| [mv/kg] | X | Y | Z |
| 1° Out of plane | -8.946340E-03 | 1.250615E-03 | -4.596133E+01 |
| 1° In plane | 4.854559E-01 | -4.651433E+01 | -4.144528E-03 |
| 2° Out of plane | 7.994077E-02 | -1.549985E-02 | 5.530611E+00 |
| 1° Torsional | -4.096249E+00 | 2.708088E-01 | 1.149119E-02 |

Fig. 4.20 Modal rotation participation factors of the SAW

The transformation matrix from the SAW2 reference frame to the **BRF** is the identity matrix, the transformation matrix from the SAW1 reference frame to the **BRF** is a 180 deg rotation around the X **BRF** axis which means that $Y_{BRF} = -Y_{SAW1}$ and $Z_{BRF} = -Z_{SAW1}$.

| SAW Modal Translation Coupling Factors | | | |
|--|---------------|---------------|---------------|
| The Solar Panel modal translation coupling factors are reported in the fully deployed configuration. | | | |
| $[\sqrt{kg}]$ | X | Y | Z |
| 1° Out of plane | -4.635139E-03 | 6.583623E+00 | 1.610784E-04 |
| 1° In plane | -1.332722E-02 | 1.718402E-03 | -6.991334E+00 |
| 2° Out of plane | 1.645563E-02 | -3.466420E+00 | -2.312155E-03 |
| 1° Torsional | 5.056233E-04 | 2.638664E-02 | 3.697665E-02 |

Fig. 4.21 Modal translation participation factors of the SAW

| Controller Parameters | Roll | Pitch | Yaw |
|-----------------------|---------|---------|------|
| K_d [N*m*sec/rad] | 20 | 115 | 70 |
| τ_z [sec] | 1 | 1 | 1 |
| K_f [rad2/sec3] | 3.6e-03 | 3.6e-01 | 0.01 |
| τ_f [sec] | 0 | 0 | 0 |
| ω_f [rad/sec] | 0.06 | 0.6 | 0.1 |
| ζ_f | 0.7 | 0.7 | 0.7 |

Fig. 4.22 SAM-EM rate controller parameters

| Controller Parameters | Roll | Pitch | Yaw |
|-----------------------|---------|---------|------|
| K_d [N*m*sec/rad] | 40 | 175 | 150 |
| K_p [N*m/rad] | 0.3 | 1.2 | 1 |
| τ_z [sec] | 1 | 1 | 1 |
| K_f [rad2/sec3] | 3.6e-03 | 3.6e-01 | 0.01 |
| τ_f [sec] | 0 | 0 | 0 |
| ω_f [rad/sec] | 0.06 | 0.6 | 0.1 |
| ζ_f | 0.7 | 0.7 | 0.7 |

Fig. 4.23 SAM-EM rate-position controller parameters

Fig. 4.24 SAM-EM angle between $-Y$ BRF axis and sun unit vector

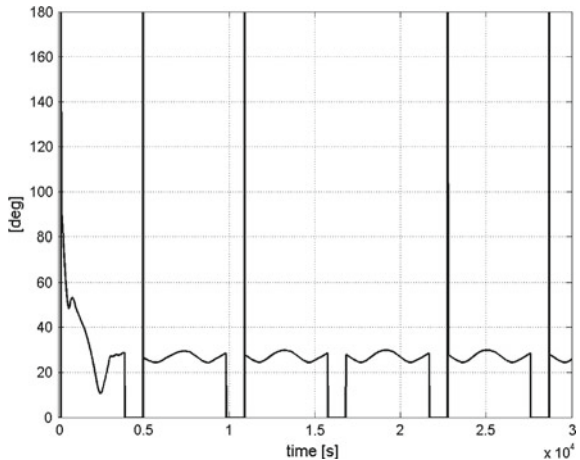
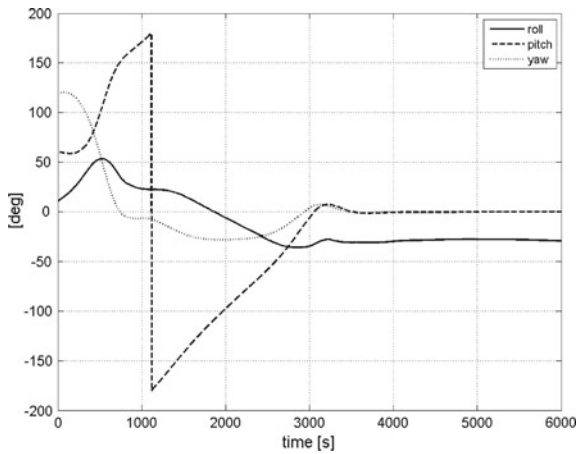


Fig. 4.25 SAM-EM attitude angles according Euler angle rotation sequence 2-1-3



The cantilevered frequencies, damping, rotational and translational participation factors of the two SAW in their SAW reference frames are shown in Figs. 4.18, 4.19, 4.20 and 4.21.

The transformation rules to transfer the modal participation factors to BRF has been discussed in Sect. 3.12.

The control gains used for the rate loop and for rate-position loop are shown in Figs. 4.22 and 4.23.

Figure 4.24 shows the behavior of the angle evaluated between $-Y$ BRF axis and the Sun unit vector in body axis during 5 orbits. This is an important indicator because the Sun has to be pointed towards the solar array wings (in this case the solar

Fig. 4.26 SAM-EM gyro measured angular rates in body axes

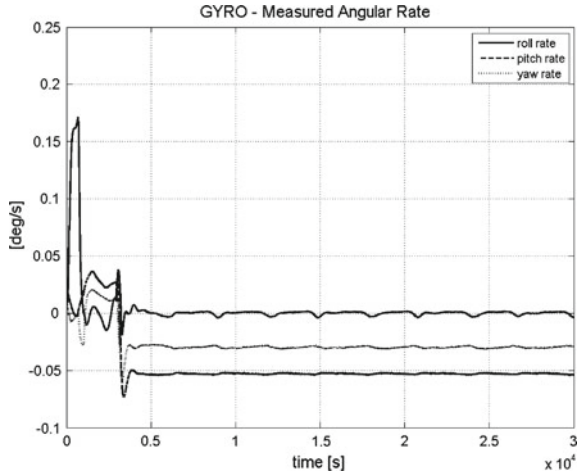
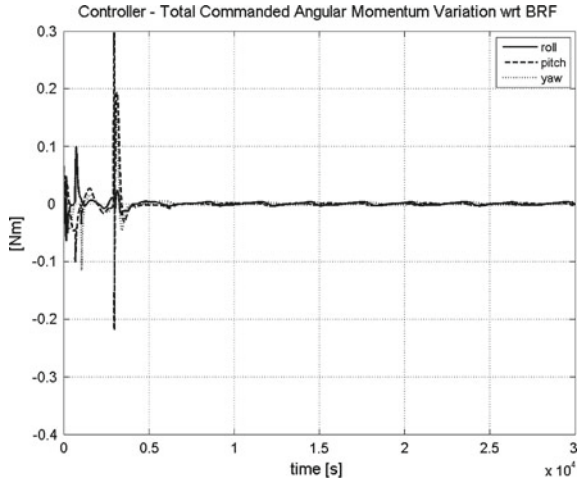


Fig. 4.27 SAM-EM RWA commanded torque in body axes



array normal is parallel to the $-Y$ BRF axis) in order to have positive power budget. The plot shows a few holes due to the presence of the eclipse. The SAM-EM mode is a PD 3-axes controlled mode, therefore the steady state pointing is maintained almost constant also during the eclipse holes due to the rate feedback control.

Figures 4.25, 4.26 and 4.27 show the evolution of satellite attitude angles, attitude rates and commanded torques.

Fig. 4.28 SAM-EM RWA angular momentum in body axes

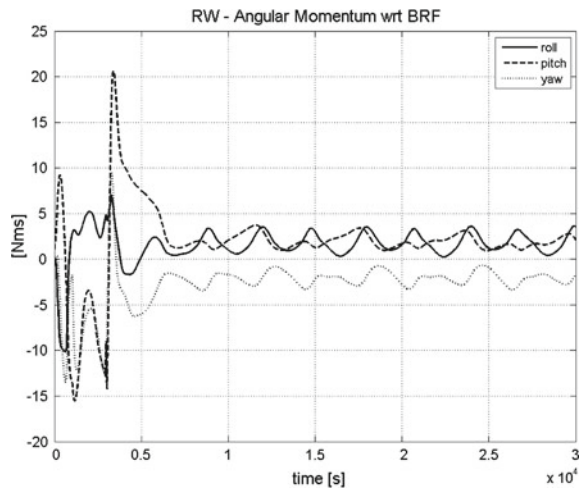
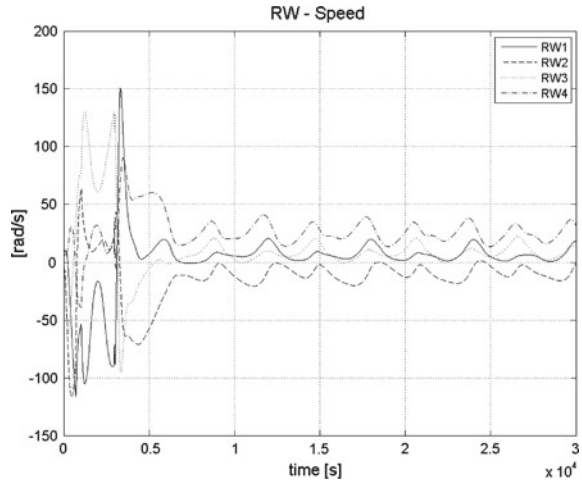


Fig. 4.29 SAM-EM RW velocity in RW axes



Finally the RWA torque and angular momentum in body axes, the RWA velocity in wheel axes and the MGT commanded momentum dipole are shown in Figs. 4.28, 4.29 and 4.30.

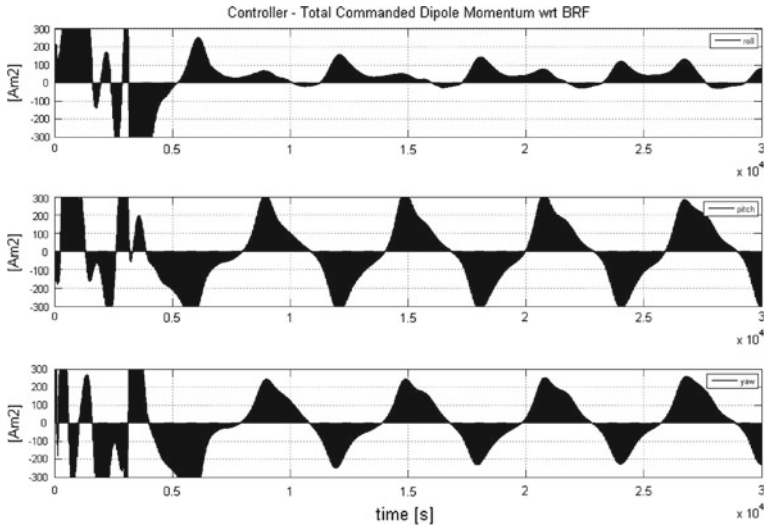


Fig. 4.30 SAM-EM MGT commanded dipole momentum in body axes

4.4.2 Safe Hold Mode

The mode is particularly effective with small satellites, microsatellites and undeployed satellites (with a low gravity gradient). The safe hold mode (SHM) implements an easy to design and test and robust approach to rate damping. This AOC mode is widely used in LEO SSO (i.e. Sun Synchronous orbit) missions because it requires a strong Earth magnetic field.

When the satellite orbit is a LEO Sun Synchronous Dawn-Dusk orbit and when the satellite has a well defined axis of maximum inertia (e.g. $-Y$ BRF), the SHM can be designed to provide also a robust Sun pointing attitude acquisition, positive power balance and thermal stability.

In such conditions the steady state attitude of this mode realizes the convergence of the maximum inertia axis to the direction orthogonal to the orbital plane, and in SSO Dawn-Dusk the Sun direction is almost orthogonal to the orbital plane. We will describe in this section the SHM for this specific orbital conditions.

The SHM is designed to support all phases of the mission (e.g. LEOP, nominal mission mode and Disposal) and it can be entered by the FDIR function when an alarm is triggered or by a ground TC when in nominal condition.

This mode uses a B -dot control law (see [15]), that is fully autonomous (no position knowledge is required), unlimited in time (there is no propellant consumption), using a limited set of highly reliable units (magnetometers, magneto-torques and reaction wheels) can be easily designed and end to end ground tested (the magnetic field is available also on the Earth surface while other sensors cannot be stimulated naturally in ground AOCS tests).

| SHM Submodes | MTQ | RW | RCT | FSS | GYRO | MGM | GPS | STT |
|--------------|-----|----|-----|-----|------|-----|-----|-----|
| Rate Damping | x | x | | x | | x | | |

Fig. 4.31 SHM mode equipments

The SHM is able to acquire the Sun from a large set of initial conditions, including any initial satellite orientation and a predefined maximum angular rates about any axis in all satellite configurations. If the selection of the magneto-torques (MGT) size is correctly carried out and the energy stored in the battery is sufficient , the Sun acquisition in any satellite configurations will be completed within a predefined worst case time typically expressed in number of orbits (typically 2 or 3 orbits) from the SHM time entry.

The following Fig. 4.31 lists AOCS hardware used to perform the attitude control.

4.4.2.1 SHM Control Loop Design

The SHM is based on a simple control law (the *B-dot*) which consists in measuring the Earth magnetic field B in **BRF** and implementing the following control law

$$m = -k\dot{B} \quad (4.39)$$

where m is the satellite magnetic dipole produced by the torquerods. The *B-dot* is part of the large family of the dissipative controllers used in *non-linear* control, which are very much used in space control.

For these controllers one aims at demonstrating stability—starting from any attitude condition- usually with the methods of the Lyapunov functions whose theory will be illustrated in Sect. 6.1.2.

The physical coupling between the dipole momentum and the external magnetic field generates the control torque that acts on the spacecraft:

$$c_c = m \times B = -k\dot{B} \times B \quad (4.40)$$

The derivative of the magnetic field in **BRF** is given by:

$$\dot{B} = M_{B \leftrightarrow E} \dot{B}_I + B \times \omega_{BE,B} \quad (4.41)$$

where \dot{B}_I is the Earth magnetic field derivative in **ECI** due to the orbital motion, while the second term is the contribution of the spacecraft spinning motion.

\dot{B}_I depends both on the variation in magnitude $|B|$ and direction e_b of the geo-magnetic field along the orbit. Considering

$$B_I = |B|e_b \rightarrow \dot{B}_I = \frac{d|B|}{dt}e_b + |B|\dot{e}_b = \frac{d|B|}{dt}e_b + \omega_{b,E} \times e_b|B| \quad (4.42)$$

where $\omega_{b,E}$ is the magnetic field rotation rate—in **ECI**- during the orbital motion:

$$\dot{e}_b = \omega_{b,E} \times e_b \quad (4.43)$$

Since the first term, related to the change of magnitude, is always parallel to the magnetic field itself, it never contributes to the *B-dot* torque so that (we indicate $M_{B \leftrightarrow E} \omega_{b,E} = \omega_b$):

$$c_c = -k(M_{B \leftrightarrow E} \dot{B}_I + B \times \omega_{BE,B}) \times B = -k(B \times (\omega_{BE,B} - \omega_b)) \times B \quad (4.44)$$

From Chap. 3 we know that the energy is an invariant in absence of gravity or magnetic torques when the momentum bias is constant (see Eq. 3.84 when flex mode have negligible effects). We then study the effect of the \dot{B} on the kinetic Energy to see if we can derive general conclusion on the dynamics. The time rate of change of kinetic energy (see 3.4) can be written as

$$\frac{d\mathcal{T}}{dt} = c_c^T \omega_{BE,B} = -k[(B \times (\omega_{BE,B} - \omega_b)) \times B]^T \omega_{BE,B} \quad (4.45)$$

For a LEO SSO dawn-dusk orbit, the Earth magnetic field can be assumed always lying in the orbit plane. Its direction variation ω_b is normal to the orbit plane with a magnitude varying in a range around twice the orbital rate, since the dipole field describes two lobes per orbit. When the spacecraft is spinning with a rate much higher than twice the orbital rate, the Earth magnetic field time derivative due to the orbital motion can be neglected.

$$|\omega_{BE,B}| \gg 2\omega_0 \rightarrow |\omega_{BE,B}| \gg |\omega_b| \quad (4.46)$$

Under this assumption, the time rate of change of kinetic energy is always less than zero, so *B-dot* acts like an energy sink, damping out the kinetic energy with a dissipative torque feedback:

$$\frac{d\mathcal{T}}{dt} \cong -k \|B \times \omega_{BE,B}\|^2 \quad (4.47)$$

Moreover when the spacecraft rate becomes of the order of magnitude of twice the orbital rate, considering that ω_b is normal to the orbit plane, while B lies in it, the time rate of change of kinetic energy \mathcal{T} is

$$\frac{d\mathcal{T}}{dt} = -k \|B \times \omega_{BE,B}\|^2 + k|B|^2 \omega_b^T \omega_{BE,B} \quad (4.48)$$

When the spacecraft angular rate is normal to the magnetic field rate, that is $\omega_{BE,B}$ lies in the orbital plane ($\omega_b^T \omega_{BE,B} = 0$), the *B-dot* law provides dissipative effects damping out the energy with the torque feedback. This energy dissipation property

provides a damping effect on the transverse dynamics (motion outside the orbital plane).

For a simple rigid body or in case of additional gyroscopic stiffness, this dissipative effect tends to damp the nutation dynamics, bringing the spacecraft to rotate around the direction of ω_b with the maximum inertia axis.

When the spacecraft rate is finally normal to the orbit plane, aligned with ω_b , the energy variation rate is given by:

$$\frac{d\mathcal{T}}{dt} = -k[(B \times (\omega_{BE,B} - \omega_b)) \times B]^T \omega_{BE,B} = -k|B|^2 \omega_{BE,B}^T (\omega_{BE,B} - \omega_b) \quad (4.49)$$

For the longitudinal dynamics the *B-dot* control law provides a torque feedback driven by the $(\omega_{BE,B} - \omega_b)$ rate error. It tends to bring the error to zero and then to bring the spacecraft rate $\omega_{BE,B}$ to be equal to the magnetic field rate ω_b (if $\omega_{BE,B} < \omega_b$ the kinetic energy begins to increase).

However, when the spacecraft is affected by a gravity gradient torque larger than the torque rods (MGT, see Chap. 9) capability, the transverse dynamics, induced by the gravity gradient, are damped by *B-dot* control law and the residual motion tends to be in the orbit plane. In this configuration the residual longitudinal motion keeps it close to the gravity gradient equilibrium attitude, with an average rate equal to the orbital one. Moreover the *B-dot* control torque variation along the orbit, because of the change of the geomagnetic field, induces a swinging motion around that equilibrium condition.

In order to achieve the sun pointing attitude with the $-Y$ **BRF** body axis sun pointing, the *B-dot* control law is used together with a fixed angular momentum polarized along the $-Y$ **BRF**. In this case the *B-dot* control law aligns the internal angular momentum to the magnetic field orbital rate. At steady state the *B-dot* control law drives the spacecraft rate to be almost equal to the magnetic field rotation rate (twice the orbital rate, two lobes per orbit).

4.4.2.2 Rate Damping Submode

The rate damping submode is used to slow down the angular rates around the three axes leaving the satellite spinning at a small rate, with the $-Y$ **BRF** body axis (maximum inertia axis) pointing toward the Sun.

As shown in the previous section a *B-dot* control law is used. The spacecraft rotational rates are damped with a commanded torque that leads the spacecraft body to synchronize with the Earth Magnetic field rate. The Earth Magnetic field has a bi-orbital component in the SSO dawn-dusk orbit, so the *B-dot* control law tries to damp the spacecraft rate to $2\omega_0$, where ω_0 is the orbital rate.

The rate damping *B-dot* control law will be applied in two different situations:

- *satellite with low gravity gradient torque configuration*: The *B-dot* control law is used together with a momentum polarized on wheel assembly. The *B-dot* law induces the alignment of internal angular momentum with the magnetic field rota-

tion rate. Loading a fixed angular momentum on the $-Y$ **BRF** axis (maximum inertia axis) of the **BRF** triad, at the end of the transient phase, the $B\text{-dot}$ control law guarantees that this axis is aligned with the orbit normal (nominal Sun pointing attitude).

- *satellite with high gravity gradient torque configuration* : The satellite rate de-spin is obtained with a $B\text{-dot}$ control law, but the large gravity gradient disturbance torque is much higher than the control torque provided by magnetic torque rods. This means the spacecraft is not able to follow the Earth magnetic field, and the gravity gradient forces the spacecraft to point its minimum inertia axis toward the Earth (i.e. $+X$ **BRF** or $-X$ **BRF** axis toward the Earth) with a pitch rotation rate that is almost equal to the ω_0 orbital rate. In this case, instead of trying to control the large gravity gradient disturbance torque, the $B\text{-dot}$ law is modified, to ensure a reference rotation rate at ω_0 .

The primary sensor used during this phase is the magnetometer and the primary actuator is the magnetic torque rod.

The RWA is used only for momentum polarization.

The FSS are used to trigger/signal the Sun's presence but is not actively used in the loop.

Figure 4.32 shows the SHM rate damping functional flow data.

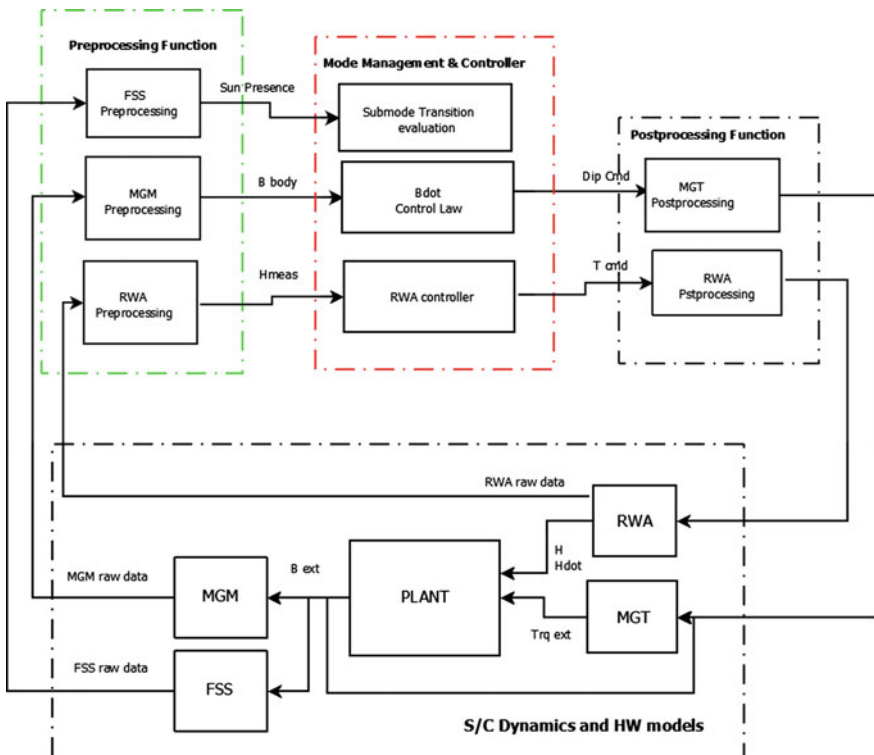


Fig. 4.32 SHM rate damping functional flow

The magnetometer raw data is processed in order to compute the three components of the B field in body axes. The B -dot control law realizes a numerical derivative of magnetic field components in order to calculate the magnetic dipole command to the Megneto-torquer (MGT) as follows:

$$m = -k \dot{B} \quad (4.50)$$

$$m_{ctrl} = m - (m^T \hat{B}) \frac{\hat{B}}{|\hat{B}|^2} = (I - \frac{\hat{B} \hat{B}^T}{|\hat{B}|^2})m \quad (4.51)$$

where \dot{B} is the derivative vector of the measured magnetic field in body reference frame, \hat{B} is the measured magnetic field unit vector in body reference frame, k is a constant gain and m_{ctrl} is the magnetic dipole momentum commanded to the MGT. In the m_{ctrl} expression the calculated dipole command m is purged from the component parallel to the magnetic field B (the term: $-(m^T \hat{B}) \frac{\hat{B}}{|\hat{B}|^2}$) to allow a saving of electric power to be made available to the components of m that are orthogonal to the magnetic field B and thus producing torque.

The physical coupling between the dipole momentum commanded to the MGT and the external magnetic field generates the control torque that acts on the spacecraft.

Due to the sensitivity of the MGM to the MGT generated magnetic field an appropriate duty cycle for their utilization has to be implemented in the real design.

In order to reduce the measurement noise a pre-filtering can be implemented to the B measurement before using this value in the B -dot calculation.

Moreover in order to avoid limit cycle between MGM measurement and MGT command a dead-band on command can be added in AOC control loop.

In rate damping submode the reaction wheels are commanded in open loop to load a predefined angular momentum in body axis.

The RWA pre-processing provides the on-board computer with accumulated angular momentum in body axes, the RWA controller calculates the RWA body axes control torque, while the RWA post-processing evaluates the torque command for each wheel starting from the torque request in body axes.

4.4.2.3 SHM Simulation

This section shows a simple simulation result for SHM as per the design solution presented in the previous sections. In particular, the simulation results are related to a S/C in stowed condition with not-null initial angular rates (i.e. after separation from launcher vehicle) during a Summer Solstice in a SSO (Sun Synchronous orbit) at an altitude of about 710 km.

The spacecraft is in stowed configuration and its inertia tensor used for the simulation is shown in Fig. 4.33.

Inertia tensor is a 3×3 matrix [kgm^2] w.r.t a body fixed frame centred in the S/C COG parallel to the mechanical build reference. [kgm^2]

| DESCRIPTION | I_{xx} | I_{yy} | I_{zz} | I_{xy} | I_{xz} | I_{yz} |
|--------------|----------|----------|----------|----------|----------|----------|
| STOWED Conf. | 2558.6 | 3135.4 | 1492.9 | -18.50 | 86.39 | 28.17 |

Fig. 4.33 Spacecraft inertia tensor in stowed configuration

Fig. 4.34 SHM angle between $-Y$ BRF axis and sun unit vector

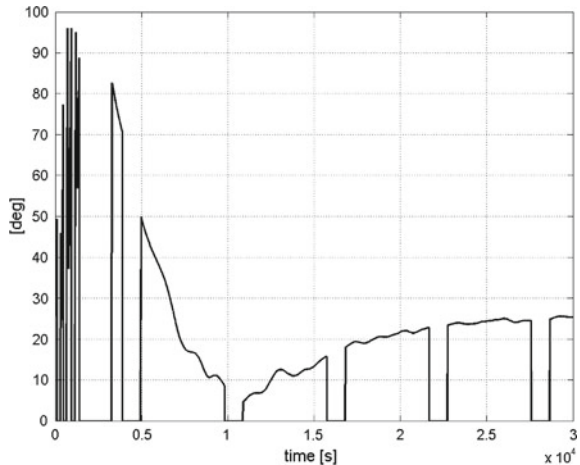
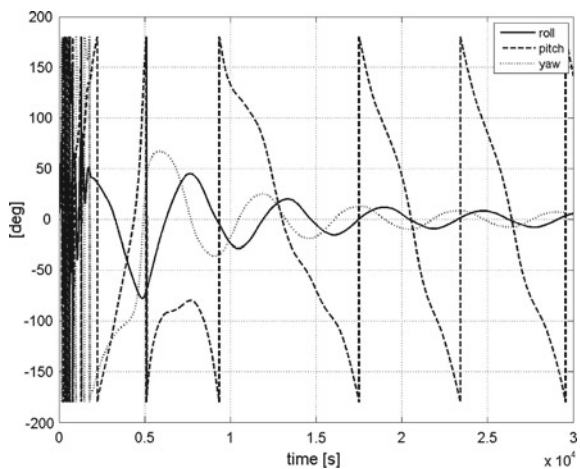


Fig. 4.35 SHM attitude angles according to Euler angle rotation sequence 2-1-3



The relevant data for the B -dot control law are: $k = 4nT/(\text{s Am}^2)$ and the MGT saturation value for the dipole momentum $m_{sat} = 300 \text{ Am}^2$.

Fig. 4.36 SHM S/C angular rate

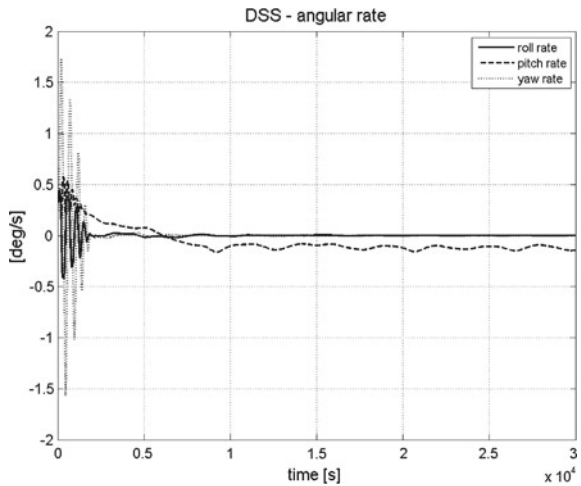
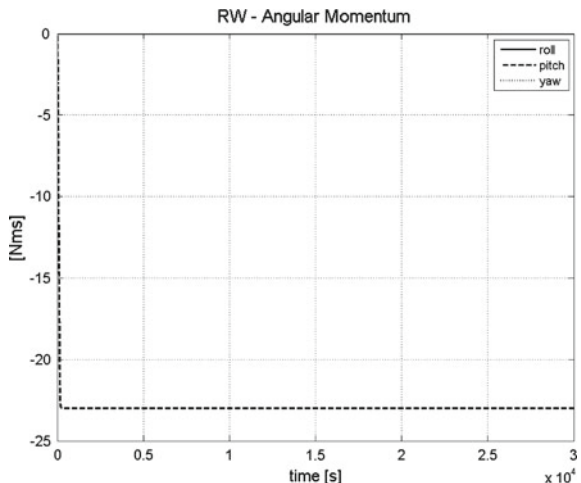


Figure 4.34 shows the behavior of the angle between $-Y$ BRF axis and the Sun unit vector. This is an important indicator because the Sun has to be pointed towards the solar array wings (in this case solar array normal is parallel to the $-Y$ BRF) in order to have positive power budget. The plot shows a few holes due to the presence of an eclipse repeated in each orbit (i.e. summer solstice simulation).

The next two Figs. 4.35 and 4.36 show the time history of attitude angles and angular rates.

Figure 4.37 shows the reaction wheel angular momentum biased at a predefined value according to the design in order to polarize a *preferred stability attitude* along $-Y$ BRF axis according to the design.

Fig. 4.37 SHM RW angular momentum in body axes



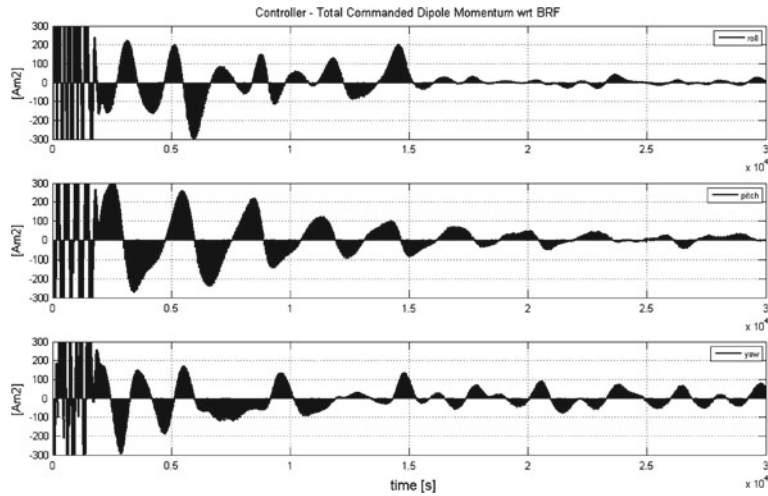


Fig. 4.38 SHM MTG commanded dipole momentum in body axes

The MGT dipole momentum behavior is shown in Fig. 4.38. It is possible to recognize the high command activity at the beginning due to the rate damping phase while when the steady state condition is reached the behavior is smoother.

Finally Fig. 4.39 shows the result of a one day simulation of SHM with a typical evolution of the Sun unit vector projected in the elevation azimuth plane.

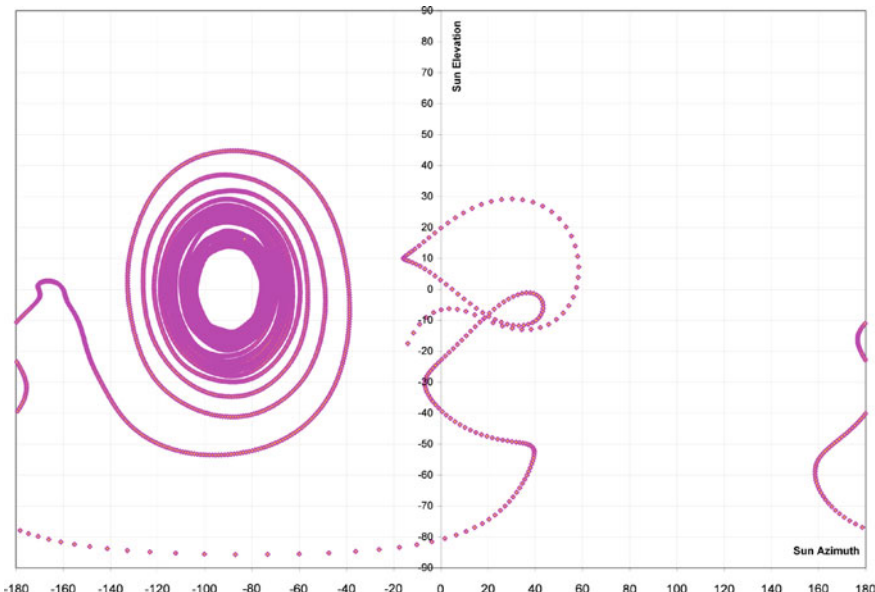


Fig. 4.39 SHM sun elevation versus azimuth evolution (1 day)

4.4.3 Normal Pointing Mode (NPM)

The NPM is designed in order to provide an attitude performance suitable for the P/L operations. The mode is entered in nominal scenarios by a ground TC from SAM-EM.

The normal mode is composed of the following submodes:

- tranquillization;
- fine pointing.

The tranquillization phase allows AOC subsystem to acquire the stable target nominal attitude as required by the mission. The controller is exactly the same in both submodes, but the bandwidth of the tranquillization submode is typically much shorter in order to avoid the controller saturation when the initial conditions at NPM are quite higher than the ones required in fine pointing.

The fine pointing submode is entered only when the attitude and rate errors are lower than the forward transition thresholds for a proper confirmation time, which avoid actuator saturation. Moreover, if in fine pointing the controller detects large attitude or rate errors, then it switches back to the tranquillization submode.

During the fine pointing submode AOC subsystem provides fine pointing accuracy and stable performance through fine attitude sensors, low disturbance actuators, stiff structure and properly designed control logic.

Figure 4.40 lists for each submode AOCS hardware used in the NPM control loop.

The NPM uses, as attitude sensors, the STT and gyro, whose data is combined in a fine attitude estimation filter. This filter smooths the measurement noise and provides the best attitude estimate available on-board. The required pointing accuracy is also ensured by the use of a precise orbit determination (POD) algorithm which provides a high precision orbital position and velocity through the on-board processing of the GNSS receiver solutions.

The NPM uses the RW for attitude control. An inertial constant external disturbance torque produces an accumulation of *angular momentum* in the RWs. This momentum must be unloaded to prevent the RW saturation. This task is realized with the use of MGT in LEO orbits and with the RCT in GEO orbits.

Moreover, the normal pointing mode provides a steering attitude ability. The steering attitude is obtained through a sequence of three elementary rotations (2-1-3 sequence) from **ORF** to **BRF**.

| NPM SubModes | MGT | RW | RCT | FSS | GYRO | MGM | GPS | STT |
|------------------|-----|----|-----|-----|------|-----|-----|-----|
| Tranquillization | + | X | | | X | | + | X |
| Fine Pointing | + | X | | | X | | + | X |

(+) HW used only in LEO ; (-) HW used only in GEO ; (x) common HW

Fig. 4.40 NPM sub mode

The Earth pointing attitude is nominally defined with roll, pitch and yaw angle equal to zero degrees.

Ground is allowed to enable/disable the Steering attitude. When the steering attitude is disabled the S/C's attitude is the Earth pointing attitude.

It is also possible to define different nominal reference attitudes depending on the specific mission (i.e. inertial reference frame, geodetic or geocentric reference frame, ...).

The NPM is designed to be robust to star sensor blinding condition (Sun, Moon, Earth) providing fine attitude control even during such events.

4.4.3.1 Fine Attitude Function

The fine attitude function is part of the attitude determination function shown in Sect. 4.3.5. This function is designed to continuously provide the NPM and OCM controllers with both attitude/rate estimate and attitude/rate reference.

The fine attitude function includes an attitude estimation filter, a smoothing function and a reference attitude generator function.

A possible implementation of an *attitude estimation filter* is described in Sect. 4.3.5.2.

4.4.3.2 Attitude Smoothing Function

The *attitude smoothing function* is in charge of ensuring a smooth transaction after a temporary unavailability of STT measurement using a dedicated weighting function to minimize the transient condition.

Given a quaternion $q_1(t)$ and a quaternion $q_2(t)$, where $q_2(t) = q_1(t) \otimes q_2(t)$, and given a predefined time period T, the smoothing function is in charge of calculating a third quaternion that verifies the following conditions:

$$\begin{cases} q_3 = q_1 & t = 0 \\ q_3 = q_2 & t = T \end{cases} \quad (4.52)$$

Providing at the same time a smooth transition from $q_1(t)$ to $q_2(t)$.

4.4.3.3 Attitude Reference Generator Function

The *attitude reference generator function* provides the NPM mode controller with reference attitude, rate and acceleration for fine pointing attitude control and S/C maneuvering (see Fig. 4.41).

S/C maneuvering is always performed using a feed forward torque compensation algorithm. The torque control law consists of two parts: the commanded feed forward torque and the angular and rate feedback.

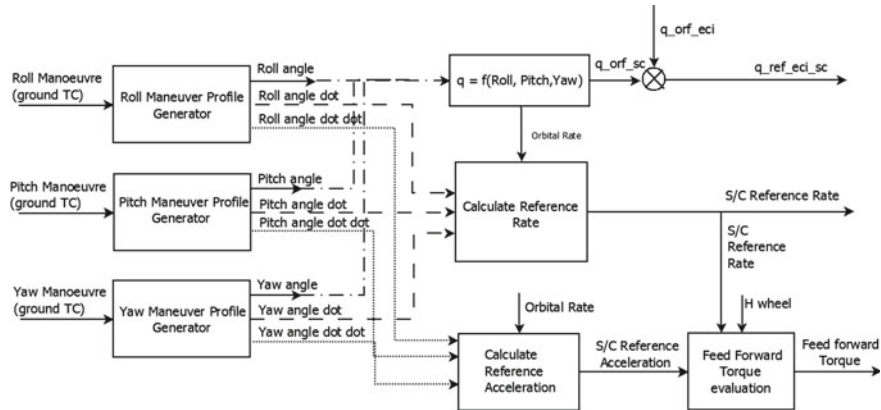


Fig. 4.41 NPM reference attitude generator

The maneuver function calculates the desired angular acceleration, rate and angular position as functions of time. The last two functions are used to feed the linear feedback system. The feed forward torque is calculated starting from the desired angular acceleration and desired angular rate.

The ground station is normally in charge of uploading, for any desired maneuver, a suitable data set which is used by the on-board software to cyclically generate, using a predefined interpolation algorithm, the following desired angular position, rate and acceleration as functions of time:

$$\begin{cases} \varphi(t), \dot{\varphi}(t), \ddot{\varphi}(t) \\ \theta(t), \dot{\theta}(t), \ddot{\theta}(t) \\ \psi(t), \dot{\psi}(t), \ddot{\psi}(t) \end{cases} \quad (4.53)$$

using, for example, the following interpolation formulas:

$$f(t) = \sum_{i=0}^5 b_i t^i + \sum_{j=1}^5 s_j \sin(\omega_j^s t) + \sum_{k=1}^5 c_k \cos(\omega_k^c t) \quad (4.54)$$

$$\dot{f}(t) = \sum_{i=0}^5 i b_i t^{i-1} + \sum_{j=1}^5 s_j \omega_j^s \cos(\omega_j^s t) - \sum_{k=1}^5 c_k \omega_k^c \sin(\omega_k^c t) \quad (4.55)$$

$$\ddot{f}(t) = \sum_{i=0}^5 i(i-1) b_i t^{i-2} - \sum_{j=1}^5 s_j \omega_j^s {}^2 \sin(\omega_j^s t) - \sum_{k=1}^5 c_k \omega_k^c {}^2 \cos(\omega_k^c t) \quad (4.56)$$

The data set which is uploaded for each maneuver and for each angle will be:

$$\begin{aligned}
 b_i & \text{ Polinomial coefficients from the 0-th to the 5-th order} \\
 s_j & \text{ Sine amplitudes} \\
 \omega_j^s & \text{ Sine angular frequencies} \\
 c_k & \text{ Cosine amplitudes} \\
 \omega_k^c & \text{ Cosine angular frequencies}
 \end{aligned} \tag{4.57}$$

Then the on-board software can calculate the reference angular rate and its derivatives using the kinematic equation presented in Sect. 2.3.2.1:

$$\boldsymbol{\omega} = \mu(\varphi, \theta, \psi) \begin{pmatrix} \dot{\varphi} \\ \dot{\theta} \\ \dot{\psi} \end{pmatrix} - M_{213}(\varphi, \theta, \psi) \omega_0 Y_{ORF} \tag{4.58}$$

where $-\omega_0 Y_{ORF}$ is the orbital rate in **ORF** which is calculated together with its derivative as a function of time using a numerical routine included in the on-board orbital propagator. Following Sect. 2.3.2.1 the angular acceleration is also obtained:

$$\begin{aligned}
 \begin{pmatrix} \dot{\omega}_1 \\ \dot{\omega}_2 \\ \dot{\omega}_3 \end{pmatrix} &= \dot{M}_{213}(\varphi, \vartheta, \psi) \begin{pmatrix} 0 \\ -\omega_0 \\ 0 \end{pmatrix} + M_{213}(\varphi, \vartheta, \psi) \begin{pmatrix} 0 \\ -\dot{\omega}_0 \\ 0 \end{pmatrix} \\
 &+ \begin{pmatrix} \ddot{\varphi} \cos(\vartheta) - \dot{\varphi} \dot{\vartheta} \sin(\vartheta) - \ddot{\vartheta} \cos(\varphi) \sin(\vartheta) + \dot{\varphi} \dot{\vartheta} \sin(\varphi) \sin(\vartheta) - \dot{\varphi} \dot{\vartheta} \cos(\varphi) \cos(\vartheta) \\ \ddot{\vartheta} + \ddot{\psi} \sin(\varphi) + \dot{\varphi} \dot{\psi} \cos(\varphi) \\ \ddot{\psi} \sin(\vartheta) + \dot{\vartheta} \dot{\psi} \cos(\vartheta) + \dot{\psi} \cos(\varphi) \cos(\vartheta) - \dot{\psi} \dot{\vartheta} \cos(\varphi) \sin(\vartheta) - \dot{\psi} \dot{\vartheta} \sin(\varphi) \cos(\vartheta) \end{pmatrix}
 \end{aligned}$$

While applying the closed loop controller output torque, calculated from the attitude error with respect to the reference attitude, it is customary to apply, at the same time (open loop feed-forward), the torque requested for the maneuver to obtain a rapid response.

Setting $\boldsymbol{\omega} = \boldsymbol{\omega}_{REF}$ we can calculate the torque which can be applied to the satellite in order to produce the desired motion, the so-called *feed forward torque*. Generally this torque is applied with a momentum management system based on reaction wheels (RW) or CMGs. In the RW case we command the RW momentum derivative so that (see Sect. 3.7 and Eq. 3.74) the satellite follows the reference kinematics:

$$-\dot{h}_{wheel} = J \dot{\omega}_{REF} + \boldsymbol{\omega}_{REF} \times J \boldsymbol{\omega}_{REF} + \boldsymbol{\omega}_{REF} \times h_{wheel} \tag{4.59}$$

This open loop control law will be more effective if $\boldsymbol{\omega}(t = 0) \approx \boldsymbol{\omega}_{REF}(t = 0)$, if the inertias used in the software are close to the actual ones and if the wheel speed measurement error is small. The attitude errors that remain after the open loop compensation will be recovered in real time through the closed loop control.

The reference attitude generator is a general purpose function that can implement a different steering law according to the mission's needs, simply by customizing the set of parameters of generic function. This structure is suitable, for example, to implement common steering laws like:

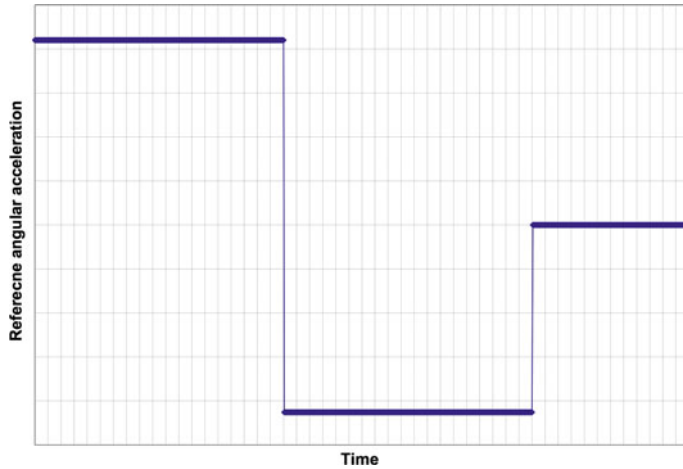


Fig. 4.42 NPM reference angular acceleration minimum time

- minimum jerk slew;
- minimum time slew.

The minimum jerk slew is used to minimize the load on actuators and avoid the actuation system to stimulate the S/C flexible modes while the minimum time slew is used to minimize the maneuver time.

As an example, hereafter we will show how the reference generator steering law can be configured to implement a minimum time slew angular acceleration profile on a single axis as shown in Fig. 4.42.

Given the acceleration function, the angular position and angular rate function can be derived, see Figs. 4.43 and 4.44:

$$\begin{cases} \alpha = a_0 + a_1 t + a_2 t^2 \\ \dot{\alpha} = a_1 + a_2 t \\ \ddot{\alpha} = a_2 \end{cases} \quad 0 \leq t \leq \frac{T}{2} \quad (4.60)$$

$$\begin{cases} \beta = b_0 + b_1 t + b_2 t^2 \\ \dot{\beta} = b_1 + b_2 t \\ \ddot{\beta} = b_2 \end{cases} \quad \frac{T}{2} \leq t \leq T \quad (4.61)$$

Assuming that the following conditions are verified:

$$\begin{cases} \alpha(0) = 0, & \dot{\alpha}(0) = 0 \\ \beta(T) = \alpha_{max}, & \dot{\beta}(T) = 0 \\ \dot{\alpha}\left(\frac{T}{2}\right) = \dot{\beta}\left(\frac{T}{2}\right) \\ \ddot{\alpha} = -\ddot{\beta} = \frac{c_{max}}{J} \end{cases} \quad (4.62)$$



Fig. 4.43 NPM reference angular rate minimum time

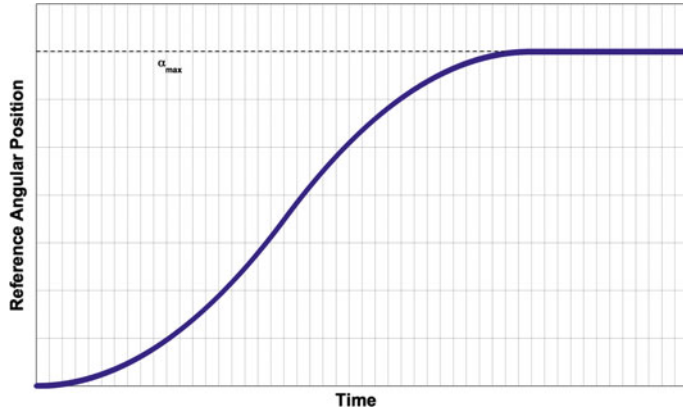


Fig. 4.44 NPM reference angular position minimum time

where J is the satellite inertia, c_{max} is the maximum torque available, α_{max} is the maximum angular position that have to be reached in the maximum time T .

The angular position coefficient can be easily calculated

$$\begin{cases} a_0 = 0, & \alpha_1 = 0, & \alpha_2 = \frac{c_{max}}{2J} \\ b_0 = \frac{c_{max}}{2J} \left(\frac{T}{2}\right)^2, & b_1 = 2(\alpha_{max} - b_0) \left(\frac{T}{2}\right)^{-1}, & b_2 = -b_1 \left(\frac{T}{2}\right)^{-2} \end{cases} \quad (4.63)$$

4.4.3.4 Tranquillization/Fine Pointing

The tranquillization submode and fine pointing submode use the same hardware and functional logic (Figs. 4.40 and 4.45).

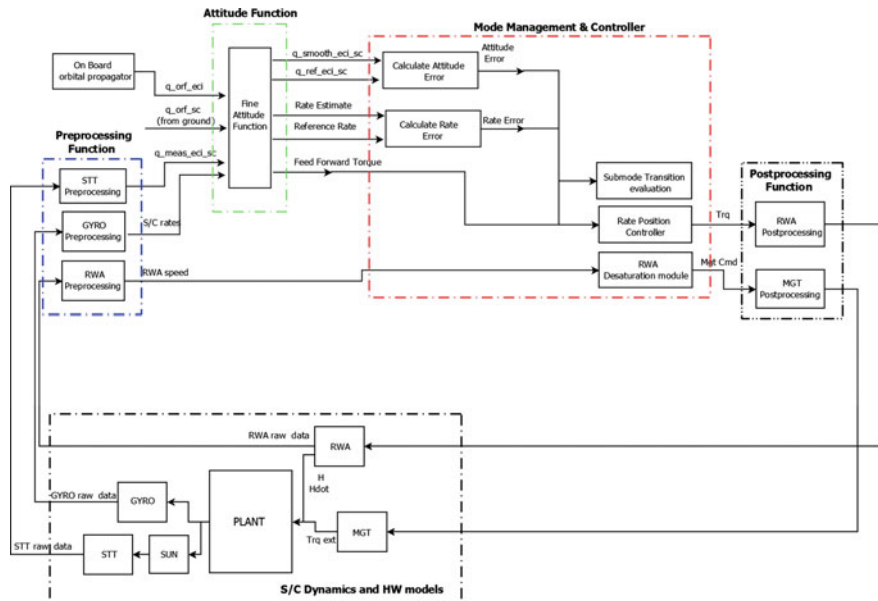


Fig. 4.45 NPM tranquillization fine pointing functional flow

The control loop gains of the two submodes are different because the NPM has to manage large initial errors and at the same time has to guarantee the fine accuracy required by the payload. To cope with these conflicting requirements, two sets of control gains have been selected: the tranquillization gains and fine pointing gains.

The first one has to guarantee the NPM convergence to the target attitude also in the presence of large initial errors maintaining the RWs in the linear torque range (no torque saturation), the steady state error of this loop is typically relaxed with respect to the required NPM performances. The second set of gains are selected to guarantee the fine attitude pointing performance starting from relatively small initial error conditions maintaining again the RWs in their linear torque range.

The fine pointing submode is entered only when attitude and rate errors are confirmed to be permanently below a given threshold, otherwise it is exited. During the transient phases the controller error normally increases, consequently the tranquillization submode is entered. When the controller operates nominally, at a steady state, the controller error remains in the fine error band and the fine pointing submode is kept.

The primary sensors used during these phases are the gyro package and the star tracker while the actuators used are the RWs. The magnetic torque rods are used only for momentum unloading.

4.4.3.5 NPM Controller Design and Stability

The NPM controller is detailed in Figs. 4.46 and 4.47. The design methods here presented will be SISO, they are applicable as already said when there is much coupling between the control axes.

Frequency methods, as already shown in the previous Sect. 4.4.1.9, are based on a combination of PID controller plus a phase-lead/phase-lag compensator and filtering, shaping the open loop gain and phase bode diagram of the overall transfer function. With reference to Fig. 4.47, calling T_{in} the input of the phase lead compensator and T_{out} the output of the structural filter—described in Fig. 4.46 by the cascade of two second order filters in space state representation \mathbf{A}_f , \mathbf{B}_f , \mathbf{C}_f , \mathbf{D}_f —the shaping is performed with the transfer function $H(s)$, such that:

$$T_{out} = H(s)T_{in} \quad (4.64)$$

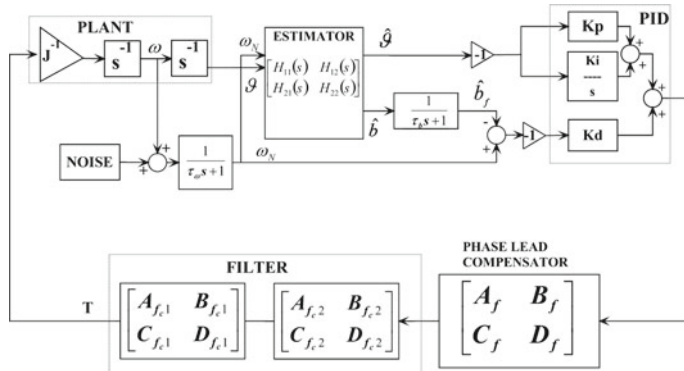


Fig. 4.46 NM single axis model

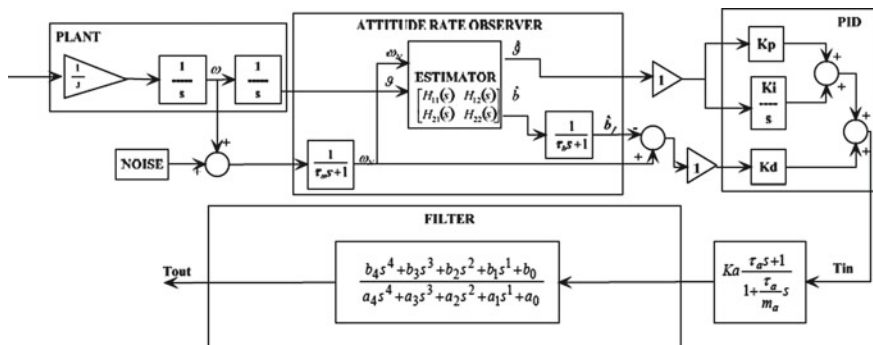


Fig. 4.47 NPM open loop system transfer function

The design goal is to guarantee at least ≈ 6 db gain margin and 30° phase margin for each body axis. The NPM controller is composed of a proportional-integral-derivative controller (PID controller), a first-order phase-lead compensator and a structural filter used to filter the flexible appendages (e.g. solar array).

All the considerations made on the plant structure in Sect. 4.4.1.9 are applicable also for the plant that has to be stabilized by NPM.

The PID controller attempts to correct the error between the attitude and rate measurement and the related references, by calculating and then exerting a torque corrective action. The PID gain has been tuned in order to provide an adequate system bandwidth to ensure good error responsiveness to fulfill the attitude pointing stability requirement. Very often, the choice to introduce an integral action is made in order to have a nominally zero error in steady state conditions in the presence of a constant disturbance torque.

The structural filter is used to filter the frequencies of the solar arrays. In this particular design where the desired bandwidth of the control loop is close to the solar array frequency (less than one decade), the design of the filter is more complicated than a classic second order filter. In general the order of the proposed filter is higher than 2nd and it does not only have poles but also zeros. In this specific case, the selected filter is a 4th order filter.

Different filter techniques can be used to achieve the desired performance in the filtering. The filter has to be synthesized with a proper selection of poles and zeros that allow it to achieve a strong amplitude reduction (more than with a simple second order filter) at a desired frequency with very low amplitude gain reduction before that frequency. The associated drawback is a strong phase reduction around the frequency bandwidth. For this reason, it is necessary to introduce a phase-lead compensator to properly manage the phase around the control bandwidth in order to achieve the desired phase margin. The typical design filter techniques are based on elliptic filters theory.

Attitude Filter Transfer Function

The attitude estimation filter, combining the gyro and the star tracker measurement (respectively ω and θ), smooths the noisy measurements and provides the best gyro drift \hat{b} as well as attitude estimate $\hat{\theta}$.

The attitude filter pass-band has been chosen in order to ensure the required pointing performance at a steady state.

Phase Lead Compensator

The phase-lead compensator transfer function can be written as follows

$$H_1(s) = K_a \frac{1 + s\tau_a}{1 + s\frac{\tau_a}{m_a}} \quad (4.65)$$

The K_a , τ_a , m_a parameters have to minimize the gain increase while ensuring a satisfactory system phase margin.

Filter Synthesis

All the identified parameters have to be selected according to a design process able to guarantee the desired performance. In particular, the low pass filter is a fourth order one introduced to filter out the flexible appendages (i.e. solar arrays). Different techniques can be used to design it, mainly related to the level of amplitude reduction and phase shaping needed at a predefined frequency. The order of this low pass filter is higher than that of the one used in the SAM-EM controller due to the fact that the desired control bandwidth is close to the flexible mode frequency, and the loop shaping must be more accurate.

In Fig. 4.48, it is possible to see a strong gain reduction (up to 27 db) at the peak of the first frequency of the solar array that guarantees a good robustness with respect to undesired flexibility effects like the spill-over that can induce loop instability.

The selection of a PID controller has been proposed to have a good steady state performance also in presence of constant or quasi-constant disturbance torques. This solution, applied to a plant that at low frequency can be considered a double integrator, requires some design attentions.

In fact, this control structure realizes a control loop chain with a good phase margin (>30 deg) but introduces a zero-dB gain crossing at low frequency (i.e. *system with conditioned stability*). In this case, a possible gain reduction in the control actuation can provide instability.

The loop design presented in Fig. 4.48 has been optimized and shows a gain margin at low frequency better than 14 db. This gain margin implies a robustness to saturation five times over the maximum torque capability of the actuator, which is normally considered sufficient.

The normal pointing mode control loop can also be designed with alternative techniques to achieve performance and stability when there is a strong coupling between the different axes (MIMO synthesis): in this case the linear control theory and linearized equations (see Sect. 3.11) can be used. For this kind of control, the linear methods are extremely powerful (see Sects. 5.4.3 and 5.5).

4.4.3.6 NPM Pointing Budget

The NPM pointing budget is carried out with the intent to evaluate the pointing attitude error during the normal pointing mode.

The NPM pointing accuracy is the deviation of the actual pointing vector from the desired pointing vector at any instant. The desired pointing vector typically refers to a payload antenna or a telescope line of sight.

The driving issues of AOCS pointing accuracy budget in this mode are the STT and gyro measurements errors and the coupling of these errors when combined in the estimation filter; moreover, the controller errors impact the pointing accuracy.

The pointing accuracy budget reports the 3σ value of the Attitude Performance Error (APE) that is defined as a difference between the commanded attitude and the actual attitude in a specified reference frame (see [16]).

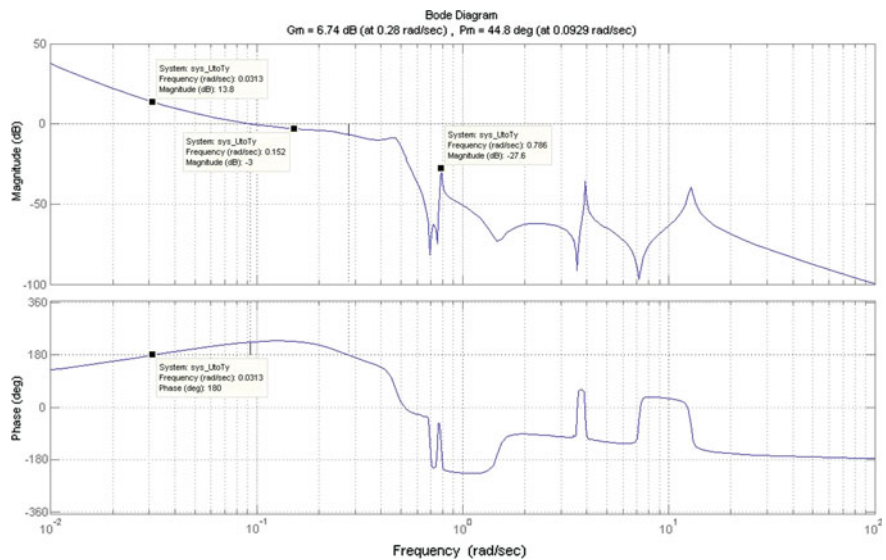


Fig. 4.48 Bode open loop chain—NPM control loop

The issues that will be dealt with in this section can also be applied to all other control loops with specific adaptations.

In order to get to the pointing error, the different error sources must be analyzed carefully.

According to [16, 17], it is possible to follow a step-by-step engineering process to obtain an attitude control pointing errors budget. The process starts with an unambiguous formulation of pointing error requirements and leads step-by-step to the evaluation of the system pointing error.

A complete and exhaustive approach can be found in [16, 17] that are used by system engineers as guidelines in all European Space Agency projects.

Usually three pointing error categories can be identified for each satellite's **BRF** axis represented by $i = 1, 2, 3$, the error sources are identified with the index j :

Bias and Drift

The bias error category includes all error sources that can be considered constant during the spacecraft's life time, and it typically includes errors like misalignment. The drift category includes all errors that vary at low rates during the mission, and errors related to aging effects are typically part of this category. Biases and drifts are summed quadratically according to [16] providing that there are no correlated errors:

$$b_i = \sqrt{3 \sum_j B_{ij}^2} \quad (4.66)$$

It is important to underline that the B_j values have to be intended as the worst case, or maximum absolute, values for each error contribution, while b_i is a statistical 3σ effective contribution of the bias class.

Harmonic

This category contains all error sources that vary with a frequency that is in the order of an orbital period. This category typically contains effects related to thermal variation during the orbit.

Harmonic errors are summed quadratically according to [16] providing that there are no correlated errors:

$$h_i = \sqrt{\frac{9}{2} \sum_j H_{ij}^2} \quad (4.67)$$

It is important to underline that the H_j values have to be intended as the worst case, or maximum absolute, values for each error contribution, while h_i is a statistical 3σ effective contribution of the harmonic class.

Random

This category contains error sources that are characterized by a high frequency behavior, typically sensor noises and actuator torque noise and vibrations are part of this category.

Random errors are summed quadratically according to [16] providing that they are all uncorrelated errors:

$$r_i = \sqrt{9 \sum_j \sigma_{ij}^2} \quad (4.68)$$

It is important to underline that the σ_j values have to be intended 1σ of the j error source.

In the total pointing budget all errors of different categories are summed quadratically:

$$\sqrt{b_i^2 + h_i^2 + r_i^2} \quad (4.69)$$

The pointing accuracy error sources of the normal pointing mode budget can be grouped into three error categories: attitude measurement errors, control errors and targeting errors.

Attitude Measurement Errors

The attitude measurement error must be calculated considering the fusion of STTs and gyro data. The AOC design foresees the implementation of the attitude estimation

filter which combines the measurement provided by the attitude sensors (STTs and gyro), thereby allowing a reduction of the STT measurement noise and the gyro drift effects.

The error sources that affect attitude measurement are presented hereafter:

- STT measurement noise and gyro measurement noise (ARW and readout noise, random),
- STT relativistic aberration, star catalog error, STT optical distortion, STT focal length error (low frequency, harmonic),
- STT focal length variation temperature (orbital frequency, harmonic),
- STT focal length variation temperature (aging, drift),
- STT internal and external misalignment (bias),
- STT ground to orbit bore-sight stability (bias),
- gyro rate bias (bias) and rate bias thermal stability (aging).

Control Errors

This term is obtained through a dynamic simulation of the S/C attitude during one orbit. The possible main sources of disturbance torques are solar disturbance, gravity gradient, MGT actuation, solar array disturbance induced by movement of the solar array to track the Sun, RWA micro-vibration induced by static and dynamic RWA imbalance, RWA torque ripple effect and dynamic disturbances due to P/L re-orientations.

Targeting Errors

The dominant contribution to this term comes from the error in the knowledge of the exact spacecraft position and time along its orbit.

When all error sources have been evaluated and classified according to the rules defined above, the overall pointing budget for NPM can be calculated.

The same approach can be extended to all other AOC modes.

4.4.3.7 NPM Simulation

This section shows a simple simulation result for NPM as per the design solutions presented in the previous sections. In particular, the simulation results are related to a S/C in fully deployed condition (i.e. all appendages deployed) during a Summer Solstice on a SSO orbit.

The spacecraft relevant data (spacecraft inertia tensor, solar array frequencies, damping, rotational and translational participation factors) used for the simulations are shown in Figs. 4.17, 4.18, 4.19, 4.20 and 4.21.

The control gains structure is shown in Fig. 4.47. The selected values are shown in Fig. 4.49.

Fig. 4.49 NPM controller parameters

| Controller Parameters | Roll | Pitch | Yaw |
|--------------------------|------------|-----------|-----------|
| K_p [N*m/rad] | 21.6537 | 119.3402 | 66.2799 |
| K_d [N*m*sec/rad] | 274.2259 | 1679.2799 | 900.9856 |
| K_i [N*m/(rad*sec)] | 0.3047 | 1.6793 | 0.901 |
| τ_a [sec] | 1 | 1 | 1 |
| τ_b [sec] | 600 | 600 | 600 |
| b4 | 0.009846 | 0.009917 | 0.00555 |
| b3 | 0.001774 | 0.001448 | 0.001079 |
| b2 | 0.03182 | 0.02632 | 0.01883 |
| b1 | 0.00008833 | 0.0006341 | 0.0005321 |
| b0 | 0.01442 | 0.01035 | 0.00864 |
| a4 | 1.0 | 1.0 | 1.0 |
| a3 | 0.432 | 0.2803 | 0.4076 |
| a2 | 0.3203 | 0.3021 | 0.2512 |
| a1 | 0.07824 | 0.05353 | 0.05593 |
| a0 | 0.01618 | 0.01462 | 0.009473 |
| K_a | 1 | 1 | 1 |
| τ_a [sec] | 7.0273 | 4.17 | 7.0273 |
| m_a | 10 | 24.9701 | 10 |

Fig. 4.50 NPM attitude angles in nominal right looking attitude with roll/yaw steering laws

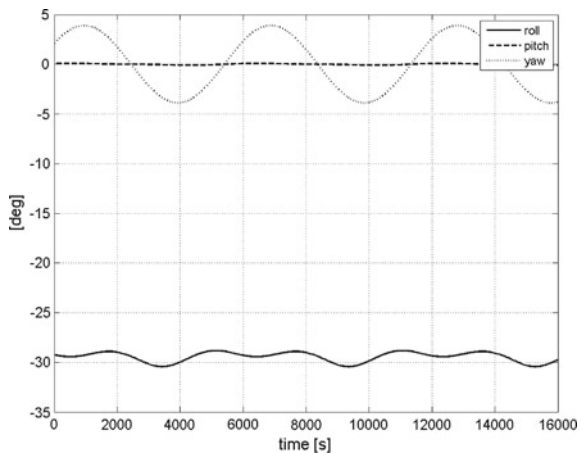


Figure 4.50 shows the behavior of NPM at steady state when the satellite is in nominal attitude (i.e. Right Looking (RL) attitude—about -30 deg in roll axis). It is possible to see that a yaw steering maneuver has been superimposed over the Right

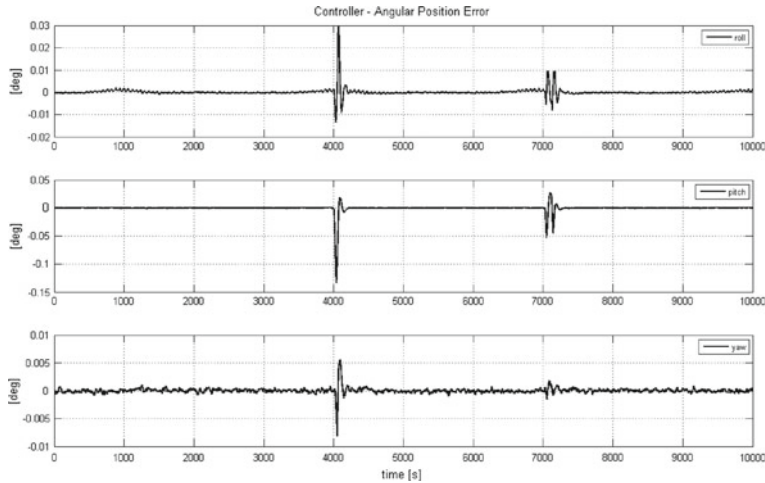


Fig. 4.51 NPM S/C attitude angle errors

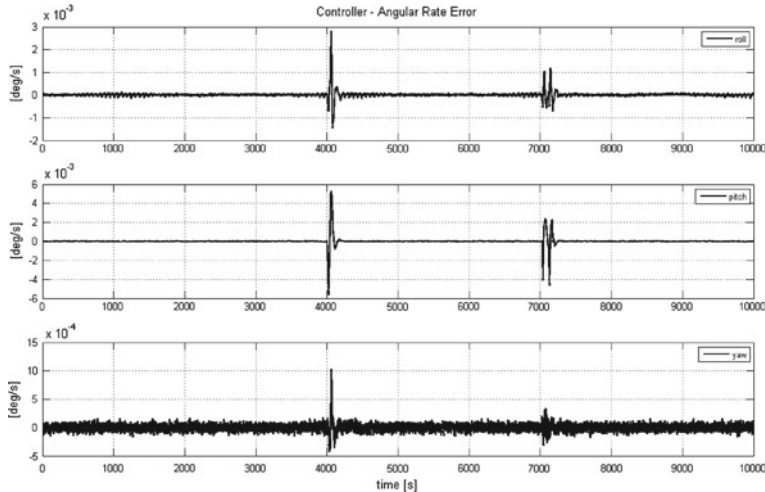


Fig. 4.52 NPM S/C angular rate errors

Looking attitude in order to support a payload need (e.g. doppler compensation). The other two Figs. 4.51 and 4.52 are related to the attitude angle errors and rate angle errors. In these two figures it is possible to see several spikes in attitude angles and angular rates due to disturbance torque induced by fast payload repointings.

Fig. 4.53 NPM RWA angular momentum in body axes

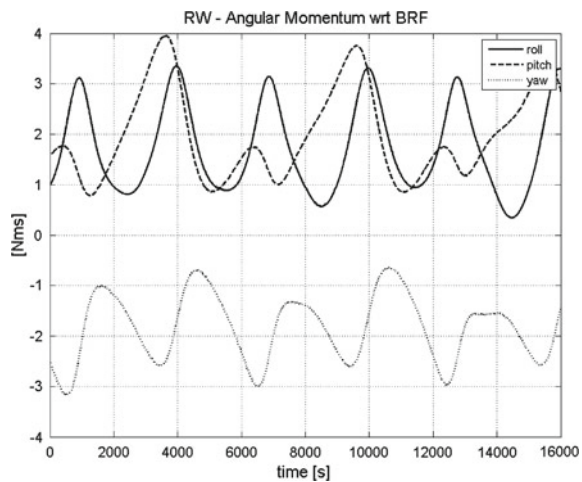
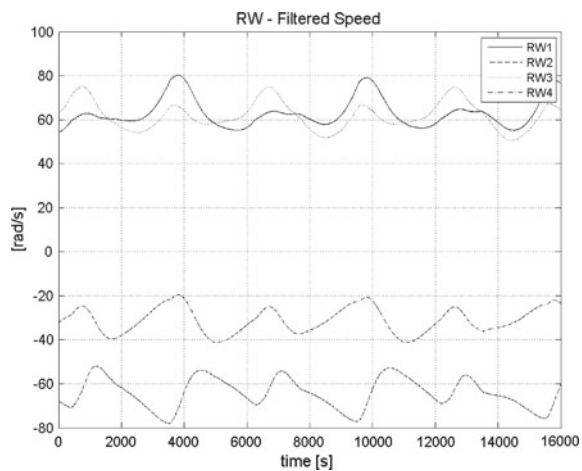


Fig. 4.54 NPM RW velocity in RW axes



Finally the RWA angular momentum in body axes, RWA velocity in wheel axes and MGT commanded momentum dipole are shown in Figs. 4.53, 4.54 and 4.55.

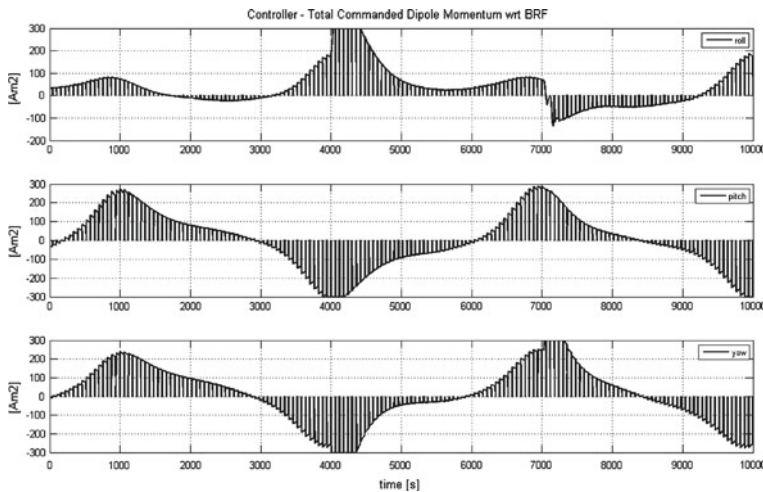


Fig. 4.55 NPM MGT commanded dipole momentum in body axes

4.4.4 Orbit Control Mode (OCM)

The OCM is used to:

- acquire the nominal orbit after launch;
- re-phase the spacecraft position on the orbit;
- correct the effect of the orbital perturbation on the desired orbital parameters;
- implement the de-orbiting maneuver at the end of the mission, in order cause the ultimate spacecraft re-entry in the Earth atmosphere. To this end extra fuel mass is budgeted in order to guarantee the necessary ΔV .

The maximum ΔT for the duration of a maneuver following a single firing has to be limited to a specific value due to the momentum build-up that results from the unavoidable misalignment of the thrust direction with respect to the spacecraft's center of mass, variable during the mission as fuel is consumed. The attitude estimator in OCM is the same used in NPM, and in fact also the attitude controller closely traces the structure of the controller used in NPM, though specific features have been included to address sloshing disturbances and RCT disturbance torques.

The orbit control mode is composed of the following submodes:

- hold mode;
- maneuver;

Figure 4.56 lists AOCS hardware used in the OCM control loop for each submode.

Hardware and functional logic of OCM submodes are the same used in NPM submodes.

The OCM mode supports the in-plane and out-of-plane orbital correction maneuvers starting from the separation from the launch vehicle, through the entire mission

| OCM SubModes | MGT | RW | RCT | FSS | GYRO | MGM | GPS | STT |
|--------------|-----|----|-----|-----|------|-----|-----|-----|
| Hold Mode | + | x | - | | x | | + | x |
| Manoeuvre | + | x | - | | x | | + | x |

(+) HW used only in LEO ; (-) HW used only in GEO ; (x) common HW

Fig. 4.56 OCM sub mode

life up to the de-orbit phase. An increase in pointing errors is generally allowed during maintenance thrusting when they have a short duration.

The OCM has been designed in order to re-gain the pointing performance within 2 min from the end of the thrust.

4.4.4.1 Hold Mode

This sub-mode is automatically entered upon transition to OCM. The entry conditions are: attitude error below a selected threshold for each axis, initial rates not exceeding a predefined threshold rate.

This sub-mode will set the spacecraft attitude in accordance to the reference quaternion up-linked from ground station, reducing the attitude and angular rate errors below predefined thresholds.

The control loop gains used in this submode can be typically the same as those used in tranquillization submode of NPM because the two submodes fulfill the same function: to damp the initial conditions to an acceptable entry condition for NPM.

4.4.4.2 Maneuver

Transition from hold mode submode to maneuver submode is triggered by a ground telecommand in order to fulfill the out-of-plane or in-plane maneuver to implement the required ΔV .

The control loop gains used in maneuver submode must be tuned to lower the attitude sensitivity to the disturbance torques induced by RCT firing during the orbital maneuver phase. Such tuning must take into account the need of stability and performance robustness (see Sect. 5.5.4).

4.4.4.3 OCM Simulation

This section shows some simulation results for OCM as per the design solution shown in the previous sections. In particular, the simulation results are related to a S/C in fully deployed condition (i.e. all appendages deployed) during the Summer Solstice in a SSO orbit with two burns performed by RCTs to simulate an orbit correction.

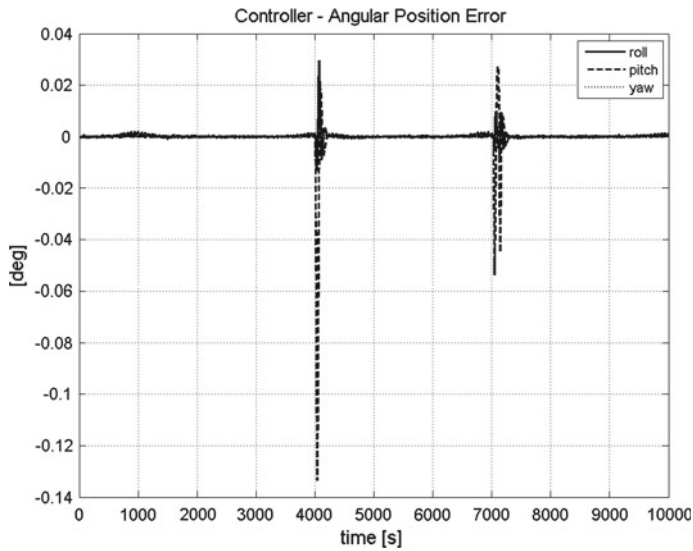


Fig. 4.57 OCM S/C attitude angle errors during RCT firings

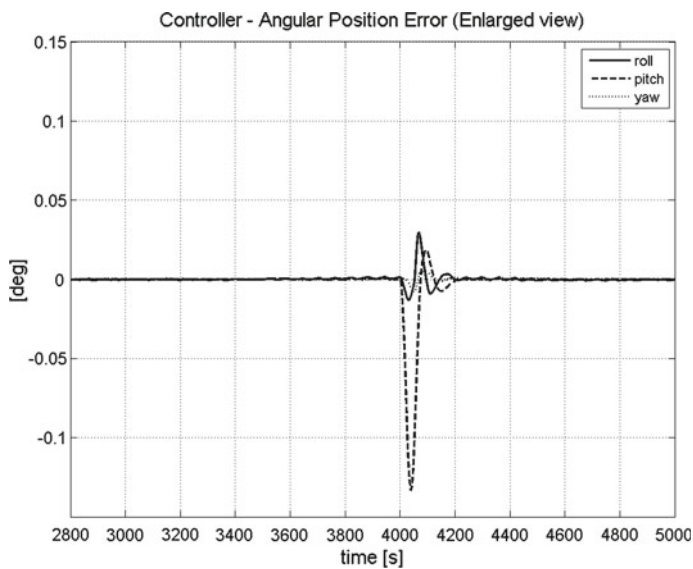


Fig. 4.58 OCM S/C attitude angle errors during RCT firing—zooming

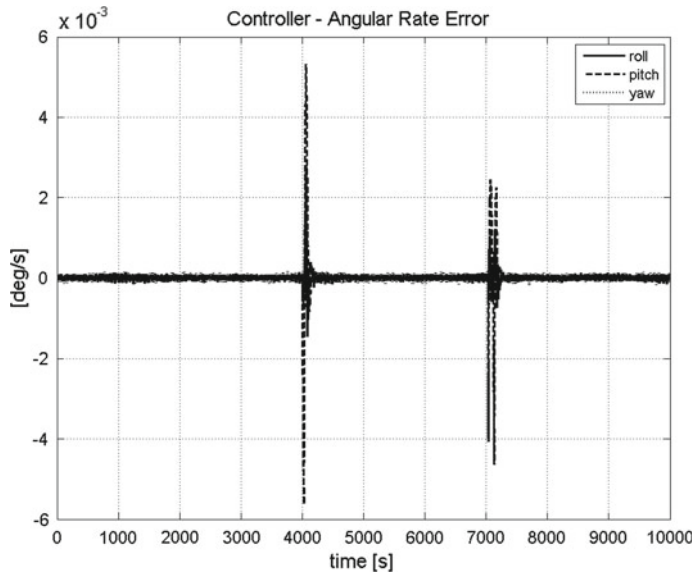


Fig. 4.59 OCM S/C angular rate errors during RCT firings

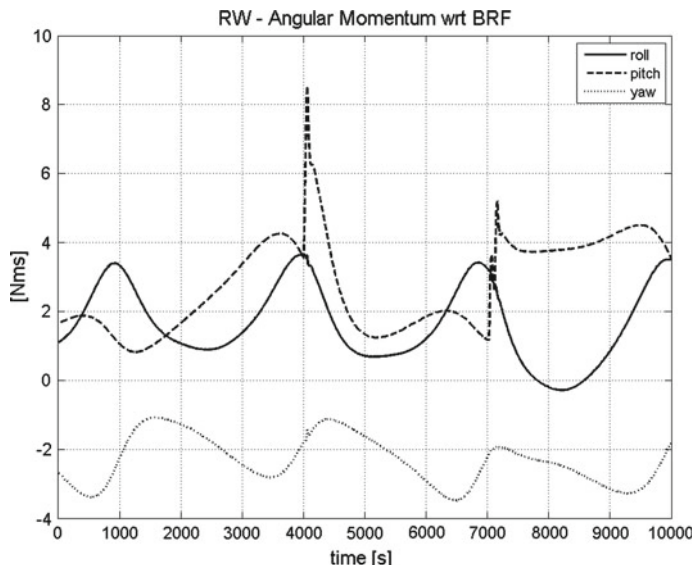


Fig. 4.60 OCM RWA angular momentum in body axes during RCT firings

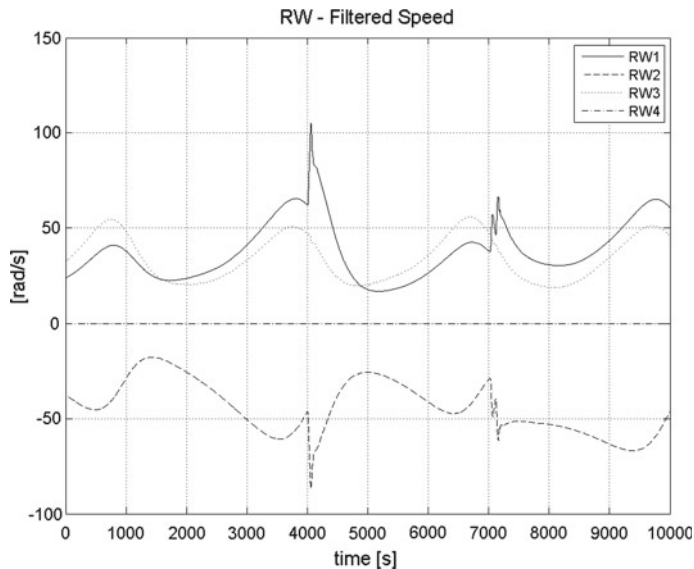


Fig. 4.61 OCM RW velocity in RW axes during RCT firings

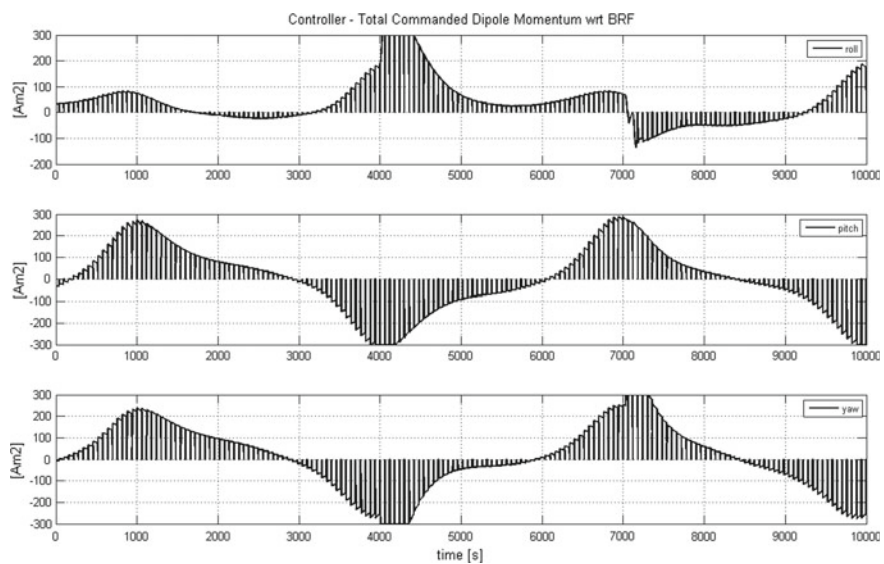


Fig. 4.62 OCM MGT commanded dipole momentum in body axes

The spacecraft relevant data (spacecraft inertia tensor, solar array frequencies, damping, rotational and translational participation factors) used for the simulations are shown in Figs. 4.17, 4.18, 4.19, 4.20 and 4.21.

The control gains used in this simulation are the same used for the NPM simulation shown in Fig. 4.49.

Figures 4.57 and 4.58 show the attitude error dynamics in OCM during a RCT firing. The second figure provide a zoom of the dynamics. Figure 4.59 shows the attitude rate errors in the same simulation.

Finally the RWA angular momentum in body axes, RWA velocity in wheel axes and MGT commanded momentum dipole are shown in Figs. 4.60, 4.61 and 4.62.

References

1. L. Mazzini, M. Surauer, in *The prospective of Integrated on-board Data System (ICDS) for Attitude Control Data Management and Platform Service: the ICDS for the ARTEMIS Satellite*, 15th International Communicatons Satellite Systems Conference, AIAA-94-1194-CP
2. B.P. Gibbs, *Advanced Kalman Filtering, Least Squares and Modeling* (Hoboken, Wiley, 2011)
3. G. Campolo, F. Cesaro, A. Intelisano, M. Pantaleoni, in *Design of the Integrated Control System, a Re-configurable Multi-Mission AOC and Data Handling Subsystem*, 6th International ESA Conference on Guidance, Navigation and Control Systems, Loutraki, Greece, 17–20 Oct 2005
4. M.D. Shuster, Three-axis attitude determination via kalman filtering of magnetometer data. J. Guidance Control Dyn. **13**(3), 506–514 (1990)
5. G. Campolo, S. Gerosa, S. Lagrasta, L. Mazzini, S. Ponzi, in *On the design of observer for attitude estimation of geosynchronous satellites*, 44th IAF, Graz, Austria, 16–22 Oct 1993
6. J.R. Wertz, *Spacecraft Attitude Determination and Control* (D. Reidel Publishing Company, Dordrecht, 2002)
7. F. Landis Markley, J.L. Crassidis, *Fundamentals of Spacecraft Attitude Determination and Control* (Springer, New York, 2015)
8. M.D. Shuster, S.D. Oh, Three-axis attitude determination from vector observations. J. Guidance Control **4**(1), 70–77 (1981)
9. M.D. Shuster, S. Tanygin, *The Many Triad Algorithms*. AAS 07-104
10. M.L. Psiaki, Extended quest attitude determination filtering. Flight mechanics symposium, NASA Goddard Space Flight Center, May 1999
11. A. Isidori, *Sistemi di Controllo*, Siderea Vol. II
12. G. Marro, *Controlli Automatici*, Zanichelli
13. B. Friedland, *Control System Design* (Mc Graw-Hill, Singapore, 1987)
14. B. Wie, C.T. Plescia, Attitude stabilization of flexible spacecraft during stationkeeping maneuvers. J. Guidance **7**(4)
15. A.C. Stickler, K.T. Alfriend, Elementary magnetic attitude control system. J. Spacecraft Rockets **13**, (1976)
16. ESSB-HB-E-003 Working Group, *ESA pointing error engineering handbook*, ESA, July 2011
17. ECSS Secretariat, *ECSS-E-ST-60-10C Space Engineering Control Performance*, ESA-ESTEC Requirements & Standards Division Noordwijk, The Netherlands, Nov 2008